Freie Universität Berlin

Department of Biology, Chemistry and Pharmacy
Institute of Chemistry and Biochemistry
Physical and Theoretical Chemistry

Master Thesis

Mechanistic investigation of CO oxidation on gold clusters deposited on defective MgO(001) surfaces

Kai Töpfer

Supervisor: Dr. Jean Christophe Tremblay
Co-Supervisor: Prof. Dr. Beate Paulus

March 17, 2015

Eidesstattliche Erklärung

Hiermit bestätige ich, Kai Töpfer, geboren am 15.02.1990 in Berlin, die Masterarbeit mit dem Thema "Mechanistic investigation of CO oxidation on gold clusters deposited on defective MgO(001) surfaces"ausschließlich unter Zuhilfenahme der in der Arbei angegebenen Quellen und Hilfsmittel angefertigt zu haben. Die Arbeit wurde bisher weder in gleicher oder ähnlicher Form oder auszugsweise noch keiner Prüfungsbehörde vorgelegt.

Berlin, den 17.03.2015

(Kai Töpfer)

Acknowledgement

First of all I would like to thank Dr. J. C. Tremblay for giving me the opportunity to write this master thesis and for the helpful support during this work and the work we have done before. Additionally, I have to give my gratitudes to Prof. Dr. B. Paulus for being my co-supervisor and for all the opportunities and support beginning with the Bachelor thesis and so on. Together with all members of our theoretical groups all of you offered me a comfortable work place for learning and researching in the field of theoretical chemistry and, last but not least, many activities I gladly remember.

Moreover, I want to thank my whole family for the care and the support during the entire Bachelor and Master and, of course, the path leading to here. Finally, a special thank goes to my friends who fill my life with fun and joy away from the work.

Contents

1 Introduction

Gold was prevented from attention as a catalyst for a long time by his property as one of the most noble metals in bulk form, until first evidence for the catalytic activity of small gold clusters were reported in the 1970s [1–3]. However, the work of Haruta et al. clearly established the exciting catalytic properties of particle sized to nanoscaled gold clusters especially for the low-temperature CO oxidation [4–6]. Many research was done to explain the high activity of gold clusters with the result of two generally accepted aspects. One aspect is the dependence of the catalytic activity on the diameter of the gold cluster, where high activity is proved for clusters with a diameter smaller than 5 nm [7]. The second one is the effect of the support material, which has a huge effect on the catalytic activity by modifying the electronic properties of the supported gold cluster [8].

The charging of the gold cluster has been found crucial for explaining the chemical reactivity. One of the smallest experimentally proven catalytic active gold cluster in the gas phase for the oxidation of CO to CO_2 is Au_2^- [9]. At surfaces the charge of small supported gold clusters is a result of electron redistribution and does highly depend on the cluster-support interaction [10]. Especially the presence of oxygen vacancies in metal-oxide supports [11–13] and underlying metal support [14] have an enormous influence on charging the gold clusters. Gold clusters on thin MgO(001) that are grown on Mo(001) or Ag(001) are well studied both by experiments [15] and theory [10]. MgO is a suitable support because of his stability and chemical inert properties as well as his comfortable handling in experiments [16]. Figure 1 shows the result of the temperature programmed reaction experiments for CO oxidation on selected Au_n clusters deposited on defect-rich MgO(001) films and the reactivity for the deposited Au_n clusters expressed as the number of formed CO_2 per cluster. So it was found a high catalytic activity for Au_8 on defect-rich MgO(001), where the charge transfer from oxygen vacancies to the gold cluster lead to an enhanced activity [11, 17]. However, a limited catalytic activity is also observed for smaller systems Au_n/MgO(001) with $n = 3 - 7$ and none for $Au_{1,2}$/MgO(001) [18].

Häkkinen et al. [20] describes qualitative properties for the catalytic activity of supported gold clusters. They include 1) dynamic structural fluxionality, that allow small cluster transformations between various energetically accessible structures to enhance the rates for overcoming reaction barriers, 2) quantum size effects, that affect the electronic structure of the gold cluster and the charge transfer from the support to the cluster. 3) impurity-doping also modifies the electronic structure of the system and consequently change chemical reactivity. The first two conditions are given for the Au_8/MgO(001) system, but for smaller gold clusters the structural fluxionality is restricted. In particular the splitting of O_2 depends on the electronic structure of the gold cluster and also on the cluster size to bond both dissociated oxygen atoms.

In this work we investigate the catalytic CO oxidation with O_2 on smaller gold clusters adsorbed on oxygen vacancies. We start with Au_2/F^{i+}-MgO(001) and Au_1/F^{i+}-MgO(001) ($i = 2, 1, 0$), which have shown no catalytic activity in the experiments and search for further explanations with regard to that property. The theoretical study based on density functional theory (DFT) using the periodic electrostatic embedded cluster method (PEECM). In this embedding scheme the system is divided into an inner local part,

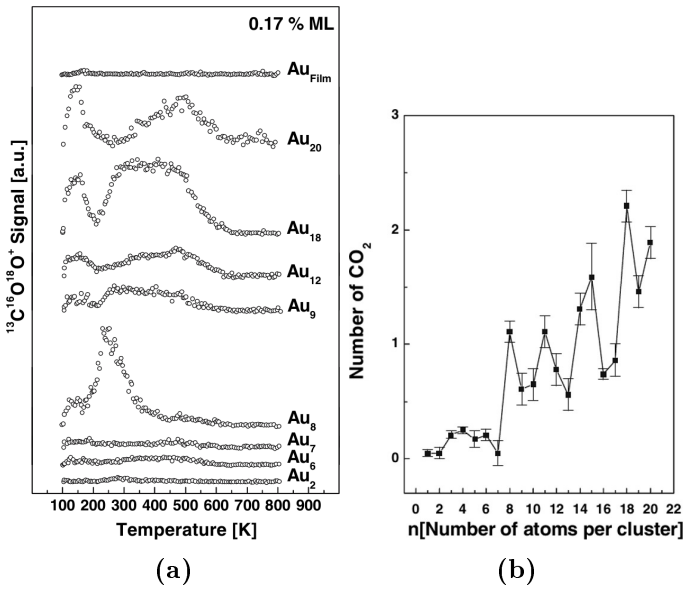

Figure 1: Results of the (a) temperature programmed reaction experiments for CO oxidation on selected Au_n clusters deposited on defect-rich MgO(001) films. The model catalysts were saturated at 90 K with ^{13}CO and $^{18}O_2$ and the isotopomer $^{13}C^{18}O^{16}O$ was detected with mass spectrometer as a function of the temperature. (b) The reactivity for Au_n clusters expressed as the number of formed CO_2 per cluster [19]. An enhanced catalytic activity is observed for Au_n clusters with a cluster size larger than $n = 8$ but none for gold films on the defect-rich MgO(001) surface. Au_n with $n = 3 - 7$ shows a small catalytic activity and no activity is observed by Au_1 and Au_2 clusters.

an intermediate part and an outer region containing a periodic array of point charges representing the cationic and anionic charge of a perfect ionic crystal. Only the inner local and intermediate part is treated quantum mechanically where the inner local region contains the small cluster with the oxygen vacancy and the gold atoms described by basis sets. In the intermediate part the cations are described by all-electron effective core potentials (ECP) and the anions by point charges. The intermediate part serves as an isolating shell for the local region against the point charges in the outer region, that prevents a too strong polarization of the electron density in the inner local region because of near positive point charges. The point charges in the outer region serves to always keep the correct electrostatic potential. This embedded cluster model is suitable for calculations on defects of ionic crystals and their surfaces. In contrast, the alternative approach with periodic boundary conditions needs large supercells to prevent a higher defect concentration than encountered in experiments, which may leads to superior interactions between neighboring defects. But larger supercells significantly increases the computational demand [21].

In this master thesis, we firstly determine the size of the intermediate part to reach convergence in system properties. Then, we investigate the adsorption behavior of CO and O_2 on Au_2 and Au_1 deposited on defective MgO(001) to get insight into the surface properties and to evaluate the suitability of the method by comparing surface properties with literature values. The last sections show the results of the investigations about reaction paths for the catalytic oxidation of CO.

2 Theory

2.1 Density Functional Theory

In quantum mechanical systems, which are described by a Hamilton operator $\hat{H}$ consisting of the operator of kinetic energy $\hat{T}$ and the operator of potential energy $\hat{V}$, the wave function ψ is determined for time-independent potentials by the non-relativistic time-independent Schrödinger equation

$$\hat{H}\psi = \left(\hat{T} + \hat{V}\right)\psi = E\psi \quad , \tag{1}$$

where the eigenvalue E corresponds to the energy of the system [22]. Without any approximations, it is not possible to analytically solve the time-independent Schrödinger equation for many-particle systems such as many-electron systems. Determining the best approximated solution is possible by using the variational principle. According to the variational principle, any normalizable test wave function ψ' yields a higher value for the energy E' then the exact energy E_0 yielding from the exact wave function of the system ψ_0. In case of $E' = E_0$, the test wave function ψ' corresponds to the exact wave function of the system.

$$\frac{\left\langle \psi' \middle| \hat{H} \middle| \psi' \right\rangle}{\langle \psi' | \psi' \rangle} = E' \geq E_0 = \frac{\left\langle \psi_0 \middle| \hat{H} \middle| \psi_0 \right\rangle}{\langle \psi_0 | \psi_0 \rangle} \tag{2}$$

Density Functional Theory (DFT) is a quantum mechanical method to investigate the electronic structure of many body systems. Contrary to the Hartree-Fock method, where wave functions are used containing all information about a quantum mechanical system, DFT determines the electronic structure with functionals depending only on the electronic density ρ. The one-electron density of a system with N electrons is defined by the integral over the spin coordinates of all electrons and over all but one spatial orbital

$$\rho(\mathbf{r}) = \mathrm{N} \int ... \int \left|\psi\left(\mathbf{x}_1 \mathbf{x}_2, ..., \mathbf{x}_n\right)\right|^2 \mathrm{d}\mathbf{s}_1 \mathrm{d}\mathbf{x}_2 ... \mathrm{d}\mathbf{x}_n \quad . \tag{3}$$

$\mathbf{x}$ represents the four-dimensional vector of the position $\mathbf{r}$ and the spin $\mathbf{s}$ of the electron. The one-electron density is the probability to find one of the N electrons with variable spin in the volume $\mathrm{d}\mathbf{x}_1$, whereby the remaining N-1 electrons can be elsewhere in the space.

Modern DFT bases on the two theorems by Hohenberg and Kohn [23]. The first theorem implies that the exact ground state energy E_0 of a system can be uniquely described by the electronic density $\rho(\mathbf{r})$ in an external potential $V_\mathrm{s}(\mathbf{r})$. The second theorem states that for every electronic density function $\rho(\mathbf{r})$, which is normalized to the number of N electrons, the variational principle is fulfilled

$$E_0 \leq E\left[\rho(\mathbf{r})\right] \quad . \tag{4}$$

2.1.1 Kohn-Sham equations

In 1965, Kohn and Sham proposed a practical method for performing DFT calculations [24]. The starting point is the electronic time-independent Schrödinger equation

$$\left(\hat{V}_{\mathrm{ee}} + \hat{V}_{\mathrm{eN}} + \hat{V}_{\mathrm{NN}} + \hat{T}_{\mathrm{e}}\right) |\phi_{\mathrm{i,R}}\rangle = \epsilon_{\mathrm{i,R}} |\phi_{\mathrm{i,R}}\rangle \quad . \tag{5}$$

Here, $\hat{V}_{\mathrm{ee}}$, $\hat{V}_{\mathrm{eN}}$ and $\hat{V}_{\mathrm{NN}}$ are the operators corresponding to the electrostatic interaction between electrons, the electrons and the nuclei as well as between the nuclei, respectively. $\hat{T}_{\mathrm{e}}$ is the operator corresponding to the kinetic energy of the electrons. The eigenfunctions $|\phi_{\mathrm{i,R}}\rangle$ and eigenvalues $\epsilon_{\mathrm{i,R}}$ are indexed by i and R as a continuous variable. However, the electronic time-independent Schrödinger equations results from the approximation that there is no coupling between the nuclear and the electronic motion, which is known as the Born-Oppenheimer approximation [25]. Kohn and Sham suggested to use a reference system of N non-interacting electrons in an external potential $V_{\mathrm{s}}(\mathbf{r})$ with the same ground state electronic density as the interacting system [26]. The Hamiltonian $\hat{H}_{\mathrm{S}}$ for the system of non-interacting electrons can be defined as

$$\hat{H}_{\mathrm{S}} = \sum_{\mathrm{i}=1}^{\mathrm{N}} \left(-\frac{1}{2}\nabla_{\mathrm{i}}^2 + V_{\mathrm{s}}(\mathbf{r}_{\mathrm{i}})\right) = \sum_{\mathrm{i}=1}^{\mathrm{N}} \hat{h}_{\mathrm{i}}^{\mathrm{KS}} \quad . \tag{6}$$

The Kohn-Sham Hamiltonian $\hat{h}_{\mathrm{i}}^{\mathrm{KS}}$ satisfies a one-electron stationary Schrödinger equation, yielding so-called Kohn-Sham orbitals $\left|\phi_{\mathrm{i}}^{KS}\right\rangle$ and energies $\epsilon_{\mathrm{i}}^{\mathrm{KS}}$

$$\hat{h}_{\mathrm{i}}^{\mathrm{KS}} \left|\phi_{\mathrm{i}}^{KS}\right\rangle = \epsilon_{\mathrm{i}}^{\mathrm{KS}} \left|\phi_{\mathrm{i}}^{KS}\right\rangle \quad . \tag{7}$$

The many-body wave function in Kohn-Sham-DFT for the non-interacting reference system ψ^{KS} is an arrangement of the Kohn-Sham orbitals in a Slater determinant to enforce the Pauli principle.

$$\psi^{\mathrm{KS}} = \frac{1}{\sqrt{\mathrm{N}}} \begin{vmatrix} \phi_1^{KS}(\mathbf{r}_1) & \phi_2^{KS}(\mathbf{r}_1) & \dots & \phi_{\mathrm{N}}^{KS}(\mathbf{r}_1) \\ \phi_1^{KS}(\mathbf{r}_2) & \phi_2^{KS}(\mathbf{r}_2) & \dots & \phi_{\mathrm{N}}^{KS}(\mathbf{r}_2) \\ \vdots & \vdots & & \vdots \\ \phi_1^{KS}(\mathbf{r}_{\mathrm{N}}) & \phi_2^{KS}(\mathbf{r}_{\mathrm{N}}) & \dots & \phi_{\mathrm{N}}^{KS}(\mathbf{r}_{\mathrm{N}}) \end{vmatrix} \tag{8}$$

In quantum theory it is postulated that the wave function must be antisymmetric with respect to the exchange of two electrons, which is fulfilled using a Slater-determinant approach [27]. This postulate is called Pauli principle or antisymmetry principle. As a

consequence of the Pauli principle, two electrons with the same spin cannot be located on the same position. Using the Kohn-Sham orbitals to represent the density of the N electron system as in equation 3, the energy of the system can be written as

$$E[\rho] = \int \rho(\mathbf{r}) V_{\mathrm{eN}}(\mathbf{r}) \mathrm{d}(\mathbf{r}) + T_{\mathrm{S}}[\rho] + \frac{1}{2} \int \int \frac{\rho(\mathbf{r_1})\rho(\mathbf{r_2})}{r_{12}} \mathrm{d}\mathbf{r_1} \mathrm{d}\mathbf{r_2} + \Delta T[\rho] + \Delta V_{\mathrm{ee}}[\rho] \ , \quad (9)$$

where $\Delta T[\rho]$ is the difference between the kinetic energy of the real system and the kinetic energy of the non-interacting system and $\Delta V_{\mathrm{ee}}[\rho]$ is defined as

$$\Delta V_{\mathrm{ee}}[\rho] = V_{\mathrm{ee}}[\rho] - \frac{1}{2} \int \int \frac{\rho(\mathbf{r_1})\rho(\mathbf{r_2})}{r_{12}} \mathrm{d}\mathbf{r_1} \mathrm{d}\mathbf{r_2} \quad , \quad (10)$$

where the second term describes the electrostatic interaction between electrons. $\Delta T[\rho]$ and $\Delta V_{\mathrm{ee}}[\rho]$ are generally unknown. Therefore an exchange-correlation functional $E_{\mathrm{XC}}[\rho]$ is defined by:

$$E_{\mathrm{XC}}[\rho] = \Delta T[\rho] + \Delta V_{\mathrm{ee}}[\rho] \quad . \quad (11)$$

The exchange-correlation functional contains the difference between the kinetic energy of the real system and the kinetic energy of the non-interacting system $\Delta T[\rho]$, the exchange energy $E_{\mathrm{X}}[\rho]$ arising from the antisymmetry requirement, and the Coulomb correlation energy $E_{\mathrm{C}}[\rho]$, which is associated with the inter-electronic repulsion. Additionally, it contains a correction for the self-interaction error. The self-interaction error arises from the Coulomb interaction of a particular electron with the charge contribution of the same electron, which makes no physical sense [28]. The exchange-correlation functional is not exactly known and must be approximated.

The effective potential $V_{\mathrm{s}}(\mathbf{r})$ in the one-electron stationary Schrödinger equation in equation 7 depends on the electronic density determined by the Kohn-Sham orbitals, which result by solving the one-electron stationary Schrödinger equation. Therefore, the Kohn-Sham orbitals are iteratively calculated by a so called self-consistent field (SCF) procedure. By choosing an initial guess for the electronic density and determining the effective potential, the SCF procedure yields in new Kohn-Sham orbitals by solving the one-electron stationary Schrödinger equation and an electronic density. The SCF procedure is iterated until convergence criteria for the Kohn-Sham orbitals and their eigenvalues are fulfilled.

2.1.2 Exchange and correlation functionals

Throughout the last decades, many different forms to the exchange-correlation functional have been proposed, which are in general categorized by the type of approximations made. The following subsection introduces the most common approximations.

Local density approximation (LDA)

The simplest approximation of the exchange-correlation functional is the local density approximation (LDA), where the inhomogeneous electron density is assumed to be a locally homogeneous electron gas. Hence, the exchange-correlation functional can be written as

$$E_{\mathrm{XC}}^{\mathrm{LDA}}[\rho] = \int \rho(\mathbf{r}) \epsilon_{\mathrm{XC}}[\rho] \mathrm{d}\mathbf{r} \quad , \tag{12}$$

where $\epsilon_{\mathrm{XC}}[\rho]$ is the exchange-correlation energy in a homogeneous electron gas. The $\epsilon_{\mathrm{XC}}[\rho]$ term corresponds to the sum of the exchange potential $\epsilon_{\mathrm{X}}[\rho]$ and the correlation potential $\epsilon_{\mathrm{C}}[\rho]$. The exchange part can easily be written as

$$\epsilon_{\mathrm{X}}[\rho] = -\frac{3}{4} \sqrt[3]{\frac{3\rho(\mathbf{r})}{\pi}} \tag{13}$$

and was originally derived by Bloch and Dirac [29]. However, there is no explicit expression for the correlation part known and thus many different correlation contributions to $\epsilon_{\mathrm{XC}}[\rho]$ are available. One widely used correlation part is the VWN functional developed by Vosko, Wilk and Nusair [29].

Generalized gradient approximation (GGA)

Additionally to the electron density $\rho(\mathbf{r})$ at point $\mathbf{r}$, the generalized gradient approximation (GGA) takes the gradient of the density $\nabla\rho(\mathbf{r})$ into account. Hence, the exchange-correlation functional can be written as

$$E_{\mathrm{XC}}^{\mathrm{GGA}}[\rho] = \int \rho(\mathbf{r}) \epsilon_{\mathrm{XC}}[\rho, \nabla\rho(\mathbf{r})] \mathrm{d}\mathbf{r} \quad . \tag{14}$$

One of the many different GGA functionals is for example the Perdew-Burke-Ernerhof functional (PBE) [30, 31] based on the PW91 functional with no empirically fitted parameters.

Hybrid functionals

Unlike LDA and GGA, hybrid functionals combine Hartree-Fock exchange energies determined with Kohn-Sham orbitals and density functional calculations. Due to a general overestimation by DFT functionals and a general underestimation by Hartree-Fock theory the combination shows in many application, but not in all, a satisfactory performance [32]. The exchange-correlation energy is defined herein by

$$E_{\mathrm{XC}}^{\mathrm{hybrid}} = \alpha E_{\mathrm{X}}^{\mathrm{HF}} + E_{\mathrm{C}} + (1-\alpha) E_{\mathrm{X}}^{\mathrm{LDA/GGA}} \quad . \tag{15}$$

The Hartree-Fock exchange energy $E_{\mathrm{X}}^{\mathrm{HF}}$ (also called exact exchange energy), the exchange energy $E_{\mathrm{X}}^{\mathrm{LDA/GGA}}$ calculated by either LDA or GGA functionals and the correlation energy E_{C} are combined by a fitting parameter α. The most widely used hybrid functional is B3LYP developed by Becke [33], Lee, Yang and Parr [34] and has the form

$$E_{\mathrm{XC}}^{\mathrm{B3LYP}} = E_{\mathrm{XC}}^{\mathrm{LDA}} + \alpha_0 \left(E_{\mathrm{X}}^{\mathrm{HF}} - E_{\mathrm{X}}^{\mathrm{LDA}}\right) + \alpha_x \left(E_{\mathrm{X}}^{\mathrm{B88}} - E_{\mathrm{X}}^{\mathrm{LDA}}\right) + E_{\mathrm{C}} + \alpha_c \left(E_{\mathrm{C}}^{\mathrm{LYP}} - E_{\mathrm{C}}^{\mathrm{LDA}}\right) \quad . \tag{16}$$

The parameters ($\alpha_0 = 0.20$, $\alpha_x = 0.72$ and $\alpha_c = 0.81$) have been determined by a fit to thermodynamical properties of a standard set of molecules. Consequently, its functional form is very well suited for determining energies and reaction barriers, which makes it a popular choice for application.

2.1.3 Unrestricted Kohn-Sham

The effective potential of the Kohn-Sham equations contains no reference to the spin of the electrons. So the approximate functionals do not differ between α- and β-spin density, only in the total density $\rho(\mathbf{r}) = \rho_\alpha(\mathbf{r}) + \rho_\beta(\mathbf{r})$ [35]. This is very suited for closed shell systems, but for systems with an arbitrary multiplicity it is appropriate to use the generalization to a spin density functional formalism, where the electron density depends on the spatial coordinates and the spin state. That results in a deviation of the spatial parts of α- and β-orbitals, because the effective potential in the one-electron Kohn-Sham equations differs between α- and β-spin orbitals, since the environments differ if there are more α- and β-electrons [36]. The advantage of this spin density functionals is to build in more of the actual physics into the approximate functionals. Furthermore it can give a proper description of bond breaking in molecules [37].

However, the single-determinant of the Kohn-Sham orbitals originating from a spin unrestricted exchange-correlation functional is not an eigenfunction of the total spin $\langle S^2 \rangle$ anymore. The eigenvalues of the total spin operator $\langle S^2 \rangle$ are calculated by S(S + 1), where S is equal to 1/2 times the number of unpaired electrons. If the $\langle S^2 \rangle$ expectation value differs from their ideal values, the determinant is described as spin contaminated. The stronger its spin contamination the more questionable the result certainly gets, because of a mixing of different spin states that results in a change of the computed total energy. In fact the single-determinant of the Kohn-Sham orbitals is not the true wave function of the system and the extent to which the spin contamination on the determinant affects the true wave function is not known [35]. In the literature some authors postulate that determinants of non-singlet systems are wrong, if they show no spin contamination [36]. Considering the system that we intend to describe is composed of a metal center on a defective insulator surface, it is to be expected that spin contamination will play an important role in our simulation.

2.1.4 Dispersion correction

Due to the local nature of the LDA and GGA functionals, they are unable to describe non-local, long range electronic correlation. This electronic correlation is crucial to describe the dispersion interaction, which is present in all atomic systems investigated here. Therefore, even hybrid functionals fails to describe dispersion correlation correctly despite their additional use of the non local Hartree-Fock exchange energy [35]. Grimme et al. firstly published an empirical dispersion correction to be improve a posteriori on DFT functionals in 2004 [38]. Such improved DFT functionals will be called DFT-Dx functionals, where x is the version number of the Grimme dispersion correction. In this work the current DFT-D3 dispersion correction is used [39]. The dispersion energy E_{disp} is simply added to the total energy E_{DFT} as

$$E_{\text{DFT-D3}} = E_{\mathrm{DFT}} + E_{\mathrm{disp}} \quad . \tag{17}$$

The empirical dispersion correction is defined by the sum of two-body-energies $E^{(2)}$ and three-body-energies $E^{(3)}$

$$E_{\mathrm{disp}} = E^{(2)} + E^{(3)} \quad , \tag{18}$$

where the two-body-energy is calculated by

$$E^{(2)} = \sum_{\mathrm{AB}} \sum_{n=6,8,10,\ldots} s_{\mathrm{n}} \frac{C_{\mathrm{n}}^{\mathrm{AB}}}{r_{\mathrm{AB}}^{\mathrm{n}}} f_{\mathrm{dmp,n}}\left(\mathrm{r_{AB}}\right) \quad . \tag{19}$$

The summation goes over all atom pairs AB in the system, $C_{\mathrm{n}}^{\mathrm{AB}}$ denotes the averaged nth order dispersion coefficient between the atom pairs with their internuclear distance r_{AB}. s_{n} are scaling factors adjusted to the DFT functional. The dispersion coefficients are computed *ab initio* by time-dependent DFT, whereby the higher order coefficients are computed recursively from the C_6^{AB} coefficients. The three-body-energy contributes with

$$E^{(3)} = \sum_{\mathrm{ABC}} f_{\mathrm{dmp,(3)}}\left(\bar{r}_{\mathrm{ABC}}\right) E^{\mathrm{ABC}} \quad , \tag{20}$$

where the sum is over all atom triplets ABC and $\bar{r}_{\mathrm{ABC}}$ is the geometrically averaged radii. The dispersion term E^{ABC} depends on the position of ABC relative to each other and a triplet dipole constant, which is approximate by a geometric mean of the two-atomic dispersion coefficients C_6^{AB} respectively.

A damping function $f_{\mathrm{dmp,n}}\left(\mathrm{r_{AB}}\right)$ is used to determine the range of the dispersion correction and to avoid near singularities and double counting effects of correlation at intermediate distances. The used function in equation 21 depends on an order-dependent

scaling factor $s_{\mathrm{r,n}}$, a cut-off radii R_0^{AB} for the atom pair AB and a steepness parameter α_{n}, which ensure that the dispersion correction at typical covalent bond length is smaller than 1 % of its maximum value of $|E_{\mathrm{disp}}|$.

$$f_{\mathrm{dmp,n}}\left(\mathrm{r_{AB}}\right) = \frac{1}{1 + 6\left(\mathrm{r_{AB}} / \left(s_{\mathrm{r,n}} R_0^{\mathrm{AB}}\right)\right)^{-\alpha_{\mathrm{n}}}} \tag{21}$$

In this work the DFT-D3 dispersion correction is used to improve the description of weakly bounded physical adsorbed states, which is important for the weak interaction between gold and molecular oxygen.

2.2 Basis set and effective core potentials

in most molecular quantum-mechanical numerical implementations of Kohn-Sham-DFT the molecular orbitals ϕ_{i} are expressed by a set of basis functions χ_{r} [28].

$$\phi_{\mathrm{i}} = \sum_{\mathrm{r}}^{\mathrm{M}} c_{\mathrm{ri}} \chi_{\mathrm{r}} \tag{22}$$

One molecular orbital ϕ_{i} is a linear combination of the M available basis functions with the respective orbital coefficients c_{ri}. Very often for molecular systems, the basis function are described by atomic-centered Gaussian type functions (GTF) as proposed by Boys in 1950 [40]. In polar coordinates the GTFs can be written as [32]

$$\chi^{\mathrm{GTF}}_{\alpha,\mathrm{nlm}}\left(r,\theta,\psi\right) = N Y_{\mathrm{lm}}\left(\theta,\psi\right) r^{2\mathrm{n}-2-\mathrm{l}} \exp^{\left(-\alpha r^2\right)} \quad . \tag{23}$$

The GTFs depend on the quantum numbers n, l, m, the spherical harmonic functions Y_{lm}, a normalization constant N and α which determines the spherical expansion. Contrary to other types of basis sets like the Slater type orbitals, a single GTFs is unable to describe the charge distribution around the nuclei accurately, but this can be improved by taking a linear combination of several GTFs centered on the same atom to generate a contracted Gaussian type function (CGTF) $\chi^{\mathrm{cGTO}}_{\alpha_1,\ldots,\alpha_{\mathrm{K}},\mathrm{nlm}}$.

$$\chi^{\mathrm{CGTF}}_{\alpha_1,\ldots,\alpha_{\mathrm{K}},\mathrm{nlm}}\left(r,\theta,\psi\right) = \sum_{\mathrm{k}=1}^{\mathrm{K}} d_{\mathrm{k}} \chi^{\mathrm{GTF}}_{\alpha_{\mathrm{k}},\mathrm{nlm}}\left(r,\theta,\psi\right) \tag{24}$$

Here, d_{k} is the contraction coefficient. Although a large number of GTFs are needed for a flexible description of the electron distribution especially for the outer region. This is more than compensated by a fast evaluation of the molecular integrals [32]. The description of the diffuse character of molecular orbitals can be improved by increasing the CGTF basis using sets of polarized and diffuse basis functions. Polarized basis functions,

whose orbital quantum number l are greater than the maximum l of the valence shell of the ground state atom, allow a distortion of the charge distribution. Diffuse functions have a very small orbital exponent and can describe electron density at large distances from the nuclei, which improve the description of electron rich systems such as anions [28].

In heavy atoms, core electrons are in fact unimportant for chemical bonding but necessary for the proper description of the valence orbitals. Thus, a large number of basis functions are required especially due to the rapidly oscillation of the radial part of the wave function [41]. The oscillation in the core region can be avoided by integrating out the core electrons and replacing them by a suitable function called effective core potential (ECP) or pseudopotential, where relativistic effects on the core electrons in heavy atoms can be treated as well. The valence electrons are still treated explicitly [32]. The strong localization of the core electrons around the nucleus effectively screens the nucleus from the valence electrons, which are unable to enter the core region due to Pauli's principle. Therefore the Coulomb interaction between the nucleus and the valence electrons will be nearly canceled out and the remaining weak interactions are described by the effective core potentials [42]. Usually when using Gaussian type functions for describing the valence electron orbitals, the effective core potentials are also described by Gaussian type functions as well [32]. This renders their evaluation very efficient while reducing drastically the computational effort associated with the electronic structure calculation.

2.3 Periodic electrostatic embedded point charge method

In the periodic electrostatic embedded point charge method (PEECM) [21] a finite, quantum mechanical cluster is embedded in a periodic, infinite array of point charges to yield the correct electrostatic potential (Madelung potential) inside the cluster. The system is divided into an inner quantum mechanically treated region (QM region) and an outer region (PC region) described by a periodic array of point charges representing the cationic and anionic sites of a perfect ionic crystal or surface. The QM region is also divided into an inner local part, or cluster, containing for example the defect or adsorbate and an intermediate part. The inner local part is described by basis sets whereas, in the intermediate part, the anions are described by point charges and the cations by all-electron ECPs (here, all-electron means the number of electrons in the respective cations). The intermediate part prevents a too strong polarization of the electron density in the inner local part of the QM region, which would be the case if a positive point charge of the PC region was not shielded by the intermediate region.

To include the electrostatic interaction between the QM and PC region the term E^{emb} is added to the total energy

$$E^{\mathrm{emb}} = \sum_{\mu\nu}^{\mathrm{cluster}} P_{\mu\nu} F_{\mu\nu}^{\mathrm{emb}} + \sum_{\mathbf{L}}^{\mathrm{lattice}} \sum_{\mathrm{j}}^{\mathrm{UC}} \sum_{\mathrm{a}}^{\mathrm{cluster}} \frac{q_{\mathrm{j}} Z_{\mathrm{a}}}{|\mathbf{R}_{\mathrm{a}} - \mathbf{R}_{\mathrm{j}} + \mathbf{L}|} \tag{25}$$

with the density matrix $P_{\mu\nu} = \sum_{\mathrm{b}=1}^{\mathrm{cluster}} c_{\mathrm{b},\mu} c_{\mathrm{b},\nu}^{*}$, Kohn-Sham matrix elements $F_{\mu\nu}^{\mathrm{emb}}$, the lattice vector in direct space $\mathbf{L}$, the ionic point charges q_{j} with index j at the position

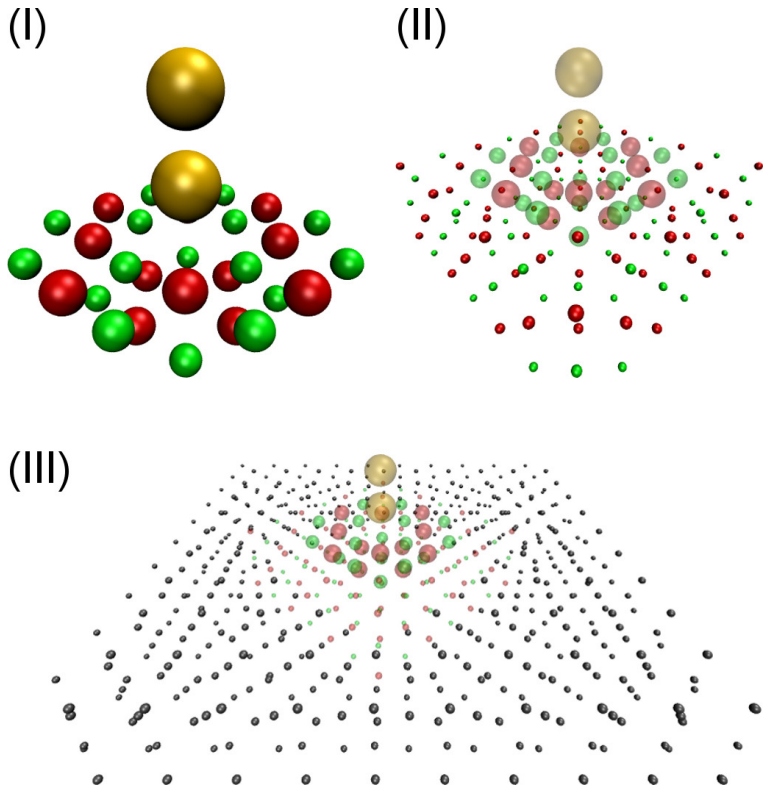

Figure 2: Illustration of the different parts with the Au_2/F^{2+}-MgO(001) system, where the Au_2 cluster is adsorbed on a F^{2+} vacancy of a MgO(001) terrace side. (I) shows the inner local part of the QM region, where the atoms are described by basis sets and also by ECPs for the Au atoms. In (II) the intermediate part surrounds the transparent inner local part. The intermediate part is treated quantum mechanically as well but the ions are described by ECP($10e^-$) for Mg^{2+} and by doubly negatively charged point charges for the O^{2-} anions. (III) shows the outer region together with the transparent QM region. In the outer region, the ions are described by point charges of $+2$ and -2 correspondingly to the ion charge. Gold (gold), magnesium (green), oxygen (red), point charges of the outer region (gray)

$\mathbf{R}_\mathrm{j} + \mathbf{L}$ outside the QM region and the nuclear charge Z_a of the atoms at the position $\mathbf{R}_\mathrm{a}$ in the QM region. μ and ν are the indices of the Gaussian basis function χ_μ and χ_ν at the position $\mathbf{R}_\mu$ and $\mathbf{R}_\nu$. The Kohn-Sham matrix elements $F_{\mu\nu}^\mathrm{emb}$ are computed by

$$F_{\mu\nu}^\mathrm{emb} = -\sum_{\mathbf{L}}^{\text{lattice}} \sum_{\mathrm{j}}^{\mathrm{UC}} q_\mathrm{j} \int \frac{\chi_\mu(\mathbf{r} - \mathbf{R}_\mu)\chi_\nu(\mathbf{r} - \mathbf{R}_\nu)\delta(\mathbf{r'} - \mathbf{R}_\mathrm{j} + \mathbf{L})}{|\mathbf{r} - \mathbf{r'}|} \mathrm{d}\mathbf{r}\mathrm{d}\mathbf{r'} \tag{26}$$

$$= -\sum_{\mathbf{L}}^{\text{lattice}} \sum_{\mathrm{j}}^{\mathrm{UC}} q_\mathrm{j} \left(\mu\nu|\delta_{\mathrm{j}\mathbf{L}}\right) \quad . \tag{27}$$

The delta function δ define the point charge q_j at the Position $\mathbf{R}_\mathrm{j} + \mathbf{L}$. The lattice sums in E^emb and $F_{\mu\nu}^\mathrm{emb}$ are calculated by the periodic fast multipole method (PFMM) [43] developed from the fast multipole method of Greengard and Rohklin [44, 45]. By partitioning the PC region into near-field and far-field parts, where the near-field is calculated analytically and the far-field by multipole expansion, the PFMM achieves a linear scaling with respect to the number of particles in computational time. PFMM defines the lattice sums entirely in direct space, which yields merely a constant shift in the electrostatic potential as compared to the Ewald method [46, 47]. Thus, the absolute energy and orbital energies have no meaning but the relative energies are unaffected provided that the total charge of the cluster remains constant.

2.4 Structure optimization

Locating stationary points on potential energy surfaces represents an important problem in computational chemistry. At stationary points the structure of a molecular system is defined by a gradient where all first derivatives with respect to all degrees of freedom (except the translational and rotational degrees of freedom) vanish. Actually stationary points include minima, maxima and transition states, which are distinguished by the eigenvalues of the second derivate of the electronic energy or Hessian matrix. A minimum is present if all eigenvalues of the Hessian matrix are positive. If the Hessian matrix contains at least one negative eigenvalue the structure corresponds to a transition states. Usually transition states where the Hessian matrix contains more than one negative eigenvalues are not of as much importance in chemistry [48].

Structure optimization are often performed using the quasi-Newton-Raphson (QNR) method [49]. Here, the gradient and an approximation of the Hessian matrix is computed. The aim is to find an energy minimum for the conformation of the molecular system. Therefore, a step vector $\Delta\mathbf{r}'$ is added to the coordinates of the atoms but in a coordinate system where the Hessian matrix is diagonal. This is achieved by a unitary transformation of the vibrational coordinates where the translational and rotational degrees of freedom are projected out prior the diagonalization [32, 50, 51]. In the case of a non-linear molecule the step vector $\Delta\mathbf{r}' = (\Delta\mathrm{r}_1, \Delta\mathrm{r}_2, ..., \Delta\mathrm{r}_{3N-6})$ is computed by

$$\Delta\mathrm{r}_i = -\frac{f_i}{\epsilon_i - \lambda} \quad , i = 1, 2, ..., 3N - 6 \tag{28}$$

where N is equal to the number of atoms, f_i are the projections of the gradient along the Hessian eigenvectors with eigenvalue ϵ_i. The shift parameter λ is chosen to be below the Hessian eigenvalue, so that the denominator in equation 28 is always positive and the step direction is always correct. However, without the implementation of the shift parameter, the step vector shifts the structure towards a saddle point or maximum if the starting point is in a region where the Hessian matrix has negative eigenvalues. Furthermore, the step parameter prevents a step size going towards infinity if an eigenvalue of the Hessian matrix comes close to zero. Usually it takes many iteration steps until the convergence criteria are fulfilled [32]. For each iteration of the QNR-algorithm an SCF calculation of the electronic structures is required. This renders structure optimization very costly.

2.5 Nudged elastic Band method

The Nudged elastic band method (NEB) serves to determine the minimal energy path (MEP) between an initial and final structure on a potential energy surface (PES). Here, multiple structures, or images, connect the initial and final state. Initially the images between initial and final state are linearly interpolate but they can also be guided by involving intermediate structures to guide the search into a certain direction [32].

The purpose of the nudged elastic band method is to minimize the force between the images of an elastic band [52, 53]. The force $\mathbf{F}_{\mathrm{i}}^{\mathrm{NEB}}$ of image i sums up the spring force $\mathbf{F}_{\mathrm{i}}^{\mathrm{s}}|_{\parallel}$ along the local and normalized tangent $\hat{\tau}_{\mathrm{i}}$ at image i and the component of the true force $\nabla E(\mathbf{R}_{\mathrm{i}})|_{\perp}$ perpendicular to the tangent $\hat{\tau}_{\mathrm{i}}$. An illustration of the forces are given in figure 3.

$$\mathbf{F}_{\mathrm{i}}^{\mathrm{NEB}} = \mathbf{F}_{\mathrm{i}}^{\mathrm{s}}|_{\parallel} - \nabla E(\mathbf{R}_{\mathrm{i}})|_{\perp} \tag{29}$$

E is the energy of the system at the atomic coordinate $\mathbf{R}_{\mathrm{i}}$ and the true force $\nabla E(\mathbf{R}_{\mathrm{i}})|_{\perp}$ is compute by subtracting out the parallel component of the true force

$$\nabla E(\mathbf{R}_{\mathrm{i}})|_{\perp} = \nabla E(\mathbf{R}_{\mathrm{i}}) - \nabla E(\mathbf{R}_{\mathrm{i}})\hat{\tau}_{\mathrm{i}} \quad . \tag{30}$$

The spring forces depend on the spring constant k and is calculated by

$$\mathbf{F}_{\mathrm{i}}^{\mathrm{s}}|_{\parallel} = k\left(|\mathbf{R}_{\mathrm{i+1}} - \mathbf{R}_{\mathrm{i}}| - |\mathbf{R}_{\mathrm{i}} - \mathbf{R}_{\mathrm{i\text{-}1}}|\right)\hat{\tau}_{\mathrm{i}} \quad . \tag{31}$$

In the original form of the NEB method the local tangent was estimated from the two adjacent images, but to avoid kinks in the minimal energy path, the local tangent at image i depends only on the adjacent image with the higher energy $E_{\mathrm{i}\pm1}$ and the image i itself [55]

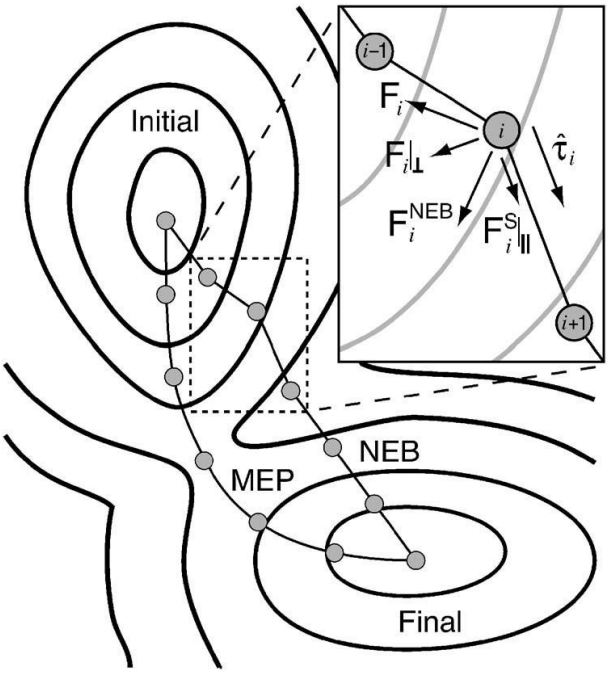

Figure 3: Forces act on the image i of the nudged elastic band (NEB) connecting the initial state with the final state. Without any restriction the image will relax towards the true force $\mathbf{F}_\mathrm{i}$. But the combination of the spring force $\mathbf{F}_\mathrm{i}^\mathrm{s}|_\parallel$ along the local tangent $\hat{\tau}_\mathrm{i}$ and the perpendicular component of the true force $\nabla E(\mathbf{R}_\mathrm{i})|_\perp = \mathbf{F}_\mathrm{i}|_\perp$ shift the image towards the force $\mathbf{F}_\mathrm{i}^\mathrm{NEB}$ in the next iteration step. If the NEB calculation converges, the band will overlap with the band along the minimal energy path (MEP). Image is taken from the Henkelman group, university of Texas at Austin [54].

$$\tau_\mathrm{i} = \begin{cases} \tau_\mathrm{i}^+ & \text{if } E_{\mathrm{i}+1} > E_\mathrm{i} > E_{\mathrm{i}-1} \\ \tau_\mathrm{i}^- & \text{if } E_{\mathrm{i}+1} < E_\mathrm{i} < E_{\mathrm{i}-1} \end{cases} \tag{32}$$

with

$$\tau_\mathrm{i}^+ = \mathbf{R}_{\mathrm{i}+1} - \mathbf{R}_\mathrm{i} \quad \text{and} \tag{33}$$

$$\tau_\mathrm{i}^- = \mathbf{R}_\mathrm{i} - \mathbf{R}_{\mathrm{i}-1} \quad . \tag{34}$$

If both adjacent images are higher or lower in energy, the tangent is computed as the weighted average of the vectors to the two neighboring images. This modification serves to smoothly switch between the two tangents τ_i^+ and τ_i^-, which can drastically change the search direction in the case of an image in a local minimum or maximum. The tangent estimate becomes

$$\tau_\mathrm{i} = \begin{cases} \tau_\mathrm{i}^+ \Delta E_\mathrm{i}^\mathrm{max} + \tau_\mathrm{i}^- \Delta E_\mathrm{i}^\mathrm{min} & \text{if } E_{\mathrm{i}+1} > E_{\mathrm{i}-1} \\ \tau_\mathrm{i}^+ \Delta E_\mathrm{i}^\mathrm{min} + \tau_\mathrm{i}^- \Delta E_\mathrm{i}^\mathrm{max} & \text{if } E_{\mathrm{i}+1} < E_{\mathrm{i}-1} \end{cases} \tag{35}$$

with

$$\Delta E_\mathrm{i}^\mathrm{max} = \max\left(|E_{\mathrm{i}+1} - E_\mathrm{i}|, |E_{\mathrm{i}-1} - E_\mathrm{i}|\right) \quad \text{and} \tag{36}$$

$$\Delta E_\mathrm{i}^\mathrm{min} = \min\left(|E_{\mathrm{i}+1} - E_\mathrm{i}|, |E_{\mathrm{i}-1} - E_\mathrm{i}|\right) \quad . \tag{37}$$

Finally the tangent vector needs to be normalized by $\hat{\tau}_\mathrm{i} = \tau_\mathrm{i}/|\tau_\mathrm{i}|$. The elastic band converges to the minimal energy path by minimizing the force of the images in equation 29 using an optimization algorithm such as the projected velocity Verlet algorithm [52]. One problem is, that none of the images lands at or near the saddle point, which energy must be estimated by interpolation a posteriori, which may yield poor estimates of activation barriers. The climbing image NEB method [55] solves that problem by identifying the image with the highest energy after a few iterations with the regular NEB method. The force on the image with the highest energy $\mathbf{F}_\mathrm{i,max}$ is then changed to

$$\mathbf{F}_\mathrm{i,max} = -\nabla E(\mathbf{R}_\mathrm{i,max}) + 2 - \nabla E(\mathbf{R}_\mathrm{i,max})|_\parallel \tag{38}$$

$$= -\nabla E(\mathbf{R}_\mathrm{i,max}) + 2 - \nabla E(\mathbf{R}_\mathrm{i,max}) \cdot \hat{\tau}_\mathrm{i,max}\hat{\tau}_\mathrm{i,max} \tag{39}$$

$\mathbf{F}_\mathrm{i,max}$ is the inverse force due to the potential and it is not affected by the string force. Now, the image moves up the potential energy surface along the elastic band while relaxing on the potential surface perpendicular to the band. As long as the climbing image NEB method converges, the climbing image will also converge to the saddle point.

2.6 MgO(001) surfaces and F-centers

Magnesium oxide MgO is a simple stoichiometric binary oxide with cubic rock-salt structure and a lattice parameter of $a = 4.211$ Å [56]. It also has well-defined surfaces, which show good stability under usual experimental conditions [57]. It is also a wide gap insulator with a large band gap of about 7.8 eV [58] and the bonding properties are highly ionic. The formal charges of Mg and O ions are very close to the nominal $+2$ and -2 values respectively [59]. The large charge separation results from the fact, that the top of the valence band formed by O 2p levels is about 9 eV below the vacuum level [60]. Thus, extracting electrons from O^{2-} has a high energy cost. The high ionic charge of O^{2-} does also only exist because of the stabilizing effect of the Madelung potential. Actually, O^{2-} will dissociate to O^- and e^- in the gas phase immediately. The Madelung potential corresponds to the electrostatic potential of a single ion in a crystal structure. This Potential is determined by the Madelung constant computed by the ratio between the average bonding energy of an ion in the crystal structure and the average bonding energy of a single ion pair. The unoccupied Mg 3s-3p level in the Mg^{2+} ions are rather closed to the vacuum level of the electron resulting in a very small electron affinity of less than 1 eV [57]. The most stable MgO(001) surface differs weakly from the bulk state. That is also shown in the low reduction of the Madelung constant of 1.747 in the bulk state to 1.681 for a 5-fold coordinated surface ion [61]. Besides, MgO(001) has a smaller band gab than the bulk state, but this is not sufficient to turn the MgO(001) surface into a chemical reactive entity [57].

One of the most important surface point defects in MgO(001) are the anion vacancies F^{i+} $(i = 2, 1, 0)$, which have a 5-fold coordination on a terrace site. F stands for Farbe center or color center meaning an anionic vacancy in a crystal or surface, where electrons can be trapped. F-centers can be created by electron bombardment on MgO(001) films

and experiments have observed a distribution of 85% F^0-, 10% F^{1+}- and 5% F^{2+}-centers, where the majority of the defects are located at the edges and the corners rather than on the regular (001) surface [57, 62]. EPR-experiments on bulk MgO shows that a trapped electron in a F^{1+} vacancy is localized in the center of the vacancy and only a fraction resides on the Mg ions [63]. The trapped electron is confined by the strong electrostatic potential of the ionic crystal. The situation is similar for the two electrons of the F^0 vacancy. Experiments [64, 65] and theoretical calculations [66, 67] shows that this properties of F-centers in the bulk does also exist on MgO(001) terrace surfaces.

Experiments of Heiz et al. adjudge F-centers a direct and important role in the activation of supported metal nanoparticles on oxide surfaces [17, 68, 69]. The investigation has shown that a different cluster size exhibits a different reactivity [17], and that this reactivity also differs for clusters or atoms deposited on defect-poor or defect-rich MgO(001) supports. In particular, a Au_8 or Pd atom deposited on defect-poor MgO(001) surfaces is essentially inert, but on defect-rich MgO(001) surfaces a clear catalytic activity is observed [17, 68]. Calculations provided evidence that the reactivity is enhanced if electron charge is transferred from the F-center to the deposited atom or cluster. The increased electronic charge on the metal atom or cluster supports the bond activation and bond breaking of adsorbents, leading to low temperature formation of products like CO_2 from CO and O_2 [17, 70].

3 Computational details

The properties of the gold clusters deposited on defective MgO(001) surfaces are studied with PEECM [21] using the *Turbomole 6.5* program package [71, 72]. DFT calculations are done with the B3LYP hybrid functional [33, 34]. The defective MgO(001) surface is created with the lattice parameter of $a = 4.211$ Å [56] by the *atomic simulation environment* [73] and the inner local part is usually represented by a $Mg_{17}O_{12}$ cluster simulating a surface terrace with a F-center. The size of the intermediate part was tested for convergence with respect to the adsorption energy of Au_2 on F^{2+}-MgO(001) and the HOMO-LUMO energy gap. The formal point charges of the Mg cations and O anions in the outer PC region and the O anions in the intermediate part of the QM region are set to +2 and −2 respectively. The Mg cations in the intermediate part are described by the 10-electron effective core potential by Hay and Wadt [74]. In the inner local region, basis sets used are 6-311G [75] on Mg and 6-31G* [76] on O, as well as 6-311++G** [77] for C and O of the adsorbents CO, O_2 and CO_2. The Au atom is described by 60-electron effective core potential of Hay and Wadt and a valence double zeta basis set [78].

To remove the basis set superposition error (BSSE) in the bimolecular complex AB with the fragments A and B, adsorption energies are counterpoise corrected [79] including monomer deformations by

$$\Delta E_{\mathrm{ads}}^{\mathrm{CP}}(\mathrm{AB}) = E_{\mathrm{AB}}^{\mathrm{AB}}(\mathrm{AB}) - E_{\mathrm{A}}^{\mathrm{A}}(\mathrm{A}) - E_{\mathrm{B}}^{\mathrm{B}}(\mathrm{B}) - E_{\mathrm{AB}}^{\mathrm{AB}}(\mathrm{A}) + E_{\mathrm{AB}}^{\mathrm{A}}(\mathrm{A}) - E_{\mathrm{AB}}^{\mathrm{AB}}(\mathrm{B}) + E_{\mathrm{AB}}^{\mathrm{B}}(\mathrm{B}) \quad (40)$$

with the adsorption or interaction energy $\Delta E_{\mathrm{ads}}^{\mathrm{CP}}(\mathrm{AB})$ of the fragments A and B, the energy of the bimolecular complex $E_{\mathrm{AB}}^{\mathrm{AB}}(\mathrm{AB})$, the energy of the fragments in the dimer basis $E_{\mathrm{AB}}^{\mathrm{A}}(\mathrm{A})$ and $E_{\mathrm{AB}}^{\mathrm{AB}}(\mathrm{B})$ and the energy of the fragments in their own basis $E_{\mathrm{AB}}^{\mathrm{A}}(\mathrm{A})$ and $E_{\mathrm{AB}}^{\mathrm{B}}(\mathrm{B})$. $E_{\mathrm{A}}^{\mathrm{A}}(\mathrm{A})$ and $E_{\mathrm{B}}^{\mathrm{B}}(\mathrm{B})$ represent the energy of fragment A and B in their own basis and optimized conformation. DFT-D3 dispersion correction [39] is enabled for the Au_1 systems and is disabled for the Au_2 systems, because the dispersion correction leads to a displacement of the top Au atom of Au_2 during structure optimizations. At structure optimizations the ions of the MgO(001) surface slab are frozen except the 8 adjacent ion of the top layer around the F-center. Harmonic frequencies of the normal modes are computed by the *NumForce* script to fix all Mg and O ions. Furthermore, a scaling factor of 0.97 is applied to all computed frequencies to take into account anharmonic effects [80]. NEB calculations are performed with *atomic simulation environment* using *Turbomole* and the *FIRE* (fast inertial relaxation engine) algorithm [81].

Illustrations of the system conformation and molecular orbitals are done with *VMD 1.9* [82, 83] and the *orbkit 0.2.0* program package [84]. Spin densities are created by *gOpenMol 3.0* [85] and graphs are generated by *gnuplot 4.6* [86]. In case, images are edited by *GIMP 2.8* [87].

4 Results and Discussion

In the following we first determine a proper system size of a Au_2 cluster deposited on defective F^{2+}-MgO(001). Therefore we look at which size for the intermediate part properties like the adsorption energies or the HOMO-LUMO-gap converge. Afterwards we investigate the adsorption behavior of a single CO or O_2 molecule on Au_2 and Au_1 clusters deposited on different charged defective Mg(001) surfaces. The results helps us to prepare possible starting structures of co-adsorbed systems and final or even transition structures for possible reaction paths. At the end nudged elastic band calculations help us to find reaction paths and to evaluate activation barriers for various investigated systems.

4.1 Preparation on the Au_2/F^{2+}-MgO(001)-system

At first we study the convergence of the QM region with respect to its size. The cluster in the inner local part is taken by the work of Pacchioni et al. [88] and simulates a oxygen vacancy in the middle of the $Mg_{19}O_{12}$-cluster. The size of the intermediate part that separates the inner local part from the point charges in the outer region is chosen by the convergence behavior of the adsorption energy of Au_2 on the oxygen vacancy as well as the convergence behavior of the HOMO-LUMO-gap. The size of the system is described by the number of atoms in each direction. The local cluster has a size of 5 atoms in the two directions parallel to the surface and 2 atomic layers in the direction of the surface normal. Therefore, it is to be expected that the adsorption energy of the Au_2 converged not until one atomic layer of the intermediate part separates the inner local part from the surrounding point charges in each direction except along the upper direction. The counterpoise corrected adsorption energy as a function of the cluster size is given in table 1.

Convergence is reached if at least one layer is isolating the local region. The same convergence behavior is observed for the width of the HOMO-LUMO-gap that are given in table 2. The HOMO-LUMO-gap of the converged systems nevertheless depends on the number of layers, where an alternation between odd and even numbers of layers seems to exist. But this alternation will converge with higher numbers of the atomic layers. In the further calculations the cluster size of the quantum mechanically treated part of $7 \times 7 \times 3$ is chosen if nothing else is mentioned.

The HOMO and LUMO of Au_2/F^{2+}-MgO(001) are shown in figure 4. The system is in the singlet state with doubly occupied molecular orbitals. Electron density difference maps between the systems with different charged vacancies shows the same spatial orientation as the LUMO of the F^{2+}-system. That means that additional trapped electrons leads to an increase of electron density at the gold cluster and the vacancy, which goes conform with the experimental and theoretical results [64–67]. Therefore we expect different adsorption behavior of CO and O_2 on the different charged defective Au_2/MgO(001).

In some cases the size of the inner local part must be increased by the adjacent atoms in the first atomic layers, because of adsorbents who are preferably adsorbed on the clean MgO(001) surface next to the gold cluster. Thus the intermediate part is increased to

Table 1: Adsorption energy of Au_2 on F^{2+}-MgO(001) as a function of the system size of the intermediate part. The adsorption energy serves as a convergence criteria for the choice of a proper system size. Here, the adsorption energy converged if at least one atomic layer of the intermediate part separates the inner local part and the surrounding point charges of the outer region. So the size of the intermediate part is determined with 7 atoms in x- and y-direction and 3 atomic layers in the z-direction. Marked with hyphen system sizes are not calculated, because an even number of atoms in x- and y-direction leads to a non radially symmetrical system with respect to the oxygen vacancy.

E_{ads} dependent on the system size in eV		number of atomic layers 2	3	4	5
	5	0.728	0.710	0.713	0.710
	6	0.694	-	0.679	-
	7	0.660	0.644	0.646	0.644
atomic size	8	0.660	-	0.645	-
in x and y	9	0.659	0.644	0.645	0.643
direction	10	0.659	-	0.644	-
	11	0.659	0.644	0.646	*
	12	0.660	-	-	*
	13	0.659	0.644	*	*

* to many atoms for *Turbomole*

Table 2: HOMO-LUMO-Gap of Au_2/F^{2+}-MgO(001) for different sizes of the quantum chemically treated region. The convergence behavior of the HOMO-LUMO-gap is similar to the behavior of the adsorption energy with at least one atomic layer of the intermediate part between the inner local cluster and the surrounding part.

HOMO-LUMO-Gap dependent on the system size in eV		number of atomic layers 2	3	4	5
	5	1.99	2.14	2.11	2.14
	6	1.85	-	1.93	-
	7	1.83	1.95	1.92	1.95
atomic size	8	1.83	-	1.92	-
in x and y	9	1.83	1.95	1.92	1.94
direction	10	1.83	-	1.92	-
	11	1.83	1.95	1.92	*
	12	1.83	-	-	*
	13	1.83	1.95	*	*

* to many atoms for *Turbomole*

the size, that at least one atomic layer separates the inner local from the surrounding part. This extension shows no qualitative effect on molecular orbitals of the inner local part.

In the clean MgO surface the oxygen vacancy causes a distortion of the adjacent ions. The magnesium cations moves away from the vacancy towards the opposing oxygen anions by 0.239 Å (value for the closed neighboring magnesium cations in the upper layer) because of the missing attractive interactions from the defective oxygen anion. The adjacent oxygen anions comes closer to the vacancy by −0.123 Å (also only for the upper layer)

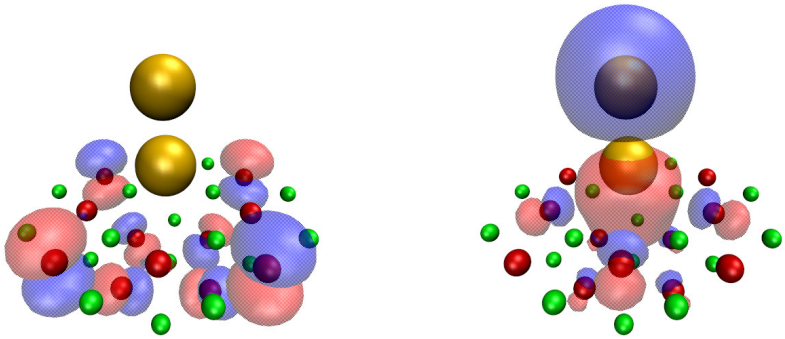

Figure 4: Isosurface for the HOMO (left) and LUMO (right) of Au_2/F^{2+}-MgO(001). The electron density of the LUMO is located at the gold atoms and the vacancy in good agreement with the electron density difference maps between the different charged systems. Due to improper visualization of *MATLAB* [89] the electron density difference map is not illustrated in this work.

because of the missing repulsive interaction from the defective oxygen anion. The weaker distortion of oxygen is reasoned by the steady coordination number and by the weaker oxygen-oxygen-interaction unlike the magnesium-oxygen-interaction. After deposition of Au_2 on the F^{2+} vacancy of the MgO(001)-surface, the deviation of the magnesium cations remains nearly constant with 0.233 Å due to a shift towards the inner of the surface. Also the oxygen anion is pushed back into the surface and away from the partial negatively charged bottom gold atom but is still -0.071 Å closer to the oxygen vacancy.

4.2 Adsorption of CO and O_2 on small supported gold cluster

4.2.1 Adsorption of CO on Au_2/F^{i+}-MgO(001)

The adsorption energies as well as the structural parameters of the different charged Au_2-CO/F^{i+}-MgO(001) systems are listed in table 3. In the work of Pacchioni et al. CO is observed to adsorb atop of the Au_2 cluster deposited on F^{2+}-MgO(001) [88]. Our calculations result in the same adsorption behavior for the systems with a F^{2+} and F^{1+} vacancy. For the uncharged charged F^0 vacancy carbon monoxide preferentially adsorbed next to the gold cluster on the MgO(001) surface. The adsorption energies of CO on Au_2 deposited on defective MgO(001) increases with the positive charge of the oxygen vacancy. The counterpoise corrected adsorption energy for Au_2-CO/F^{2+}-MgO is 1.39 eV and goes down to 0.41 eV for the F^{1+} system. In the case of the F^0-MgO(001) vacancy CO does not adsorb atop on the Au_2 cluster but the adsorption next to the Au_2 cluster on a magnesium ion leads to a metastable state with a negative adsorption energy of -0.90 eV. Experimentally determined values by temperature programmed spectroscopy (TDS) for the adsorption of CO on clean MgO(001) reaches from E_{ads}(CO/MgO(001)) = 0.14 eV

[90] to E_{ads}(CO/10 ML MgO(001)/Mo(001)) = 0.46 eV on ultrathin MgO(001) films grown on Mo(001) [91]. Here, the adsorption next to the Au_2 cluster on a magnesium ion leads to a negative adsorption energy of −0.90 eV due to the interaction between CO and Au_2 cluster. The bending state of the Au_2 cluster is 0.92 eV higher in energy than the relaxed Au_2/F^0-MgO(001) system without CO. Without involving the relaxed structures into the counterpoise correction and using the approximate correction the adsorption energy increased to 0.02 eV, which is also relatively small. But the frequency analysis shows no imaginary frequencies, therefore it is just a metastable adsorption site of CO. In general CO adsorbs stronger on cationic gold clusters and in the electron rich F^0 system the adsorption of CO on the clean MgO(001) surface is even energetically more favorable. In the case where the adsorption energy of CO atop of the gold cluster is smaller than the adsorption energy on the clean MgO(001) surface, CO adsorbs preferentially on the MgO(001) surface next to the gold cluster.

Table 3: Adsorption energies and structural parameters of the different charged Au_2-CO/F^{i+}-MgO(001). Adsorption energies are counterpoise corrected and a scaling factor of 0.970 has been applied to the computed frequencies [80].

system / Au_2-CO on	F^{2+}-MgO(001)	F^{1+}-MgO(001)	F^0-MgO(001)
adsorption behavior	atop	atop	side
E_{ads}(Au-CO) in eV	1.39	0.41	-0.90
ν(CO) in cm^{-1}	2203	2141	2099
r(Au-C) in Å	1.978	2.049	3.292 / 3.589
r(C-O) in Å	1.121	1.129	1.132
∠Au-C-O in [°]	179.0	164.2	-

Without adsorbed CO the Au_2 cluster bonds perpendicular to the surface but the adsorption of CO causes a bending of the resulting Au_2-CO cluster. Parameters like the C-O and Au-C distances or the Au-C-O angle dependent strongly on the π-back-bond from the Au 6s to the CO π^* orbital and therefore on the charge of the vacancy [92]. Hence in the system Au_2-CO/F^{2+}-MgO(001), no or a very weak π-back-bond exists because of the incompatible orbital symmetry. There is no orbital overlap between Au 6s and the CO π^* in the case of a Au-C-O angle of nearly 180°. The structure optimization results in a Au-C-O angle of 179.0°. The deviation from the linear structure is caused by the very soft bending potential for ∠Au-C-O [92]. The one additional electron in Au_2-CO/F^{1+}-MgO(001) induces a small π-back-bond, that can be seen by the smaller Au-C-O angle of 164.2°and the increased C-O distance from 1.121 Å (F^{2+} system) to 1.129 Å (F^{1+} system). The π-back-bond effects an increase of the C-O bond length by the occupation of the anti-bonding π^* orbitals, which destabilizes the C-O bond.

The adsorbed CO gets a steeper potential for the bonding elongation of C-O. The missing or very weak π-back-bond in the F^{2+} system does not destabilize the C-O bond, so that the stretch frequency ν(CO) gets a blue shift to 2203 cm^{-1} in comparison to the stretch frequency in the gas phase of 2143 cm^{-1}. The small π-back-bond in the F^{1+} system results in an equilibrium situation of both effects, so that the stretch frequency with 2141 cm^{-1} is nearly the same as in the gas phase. The C-O stretch frequencies depends highly on the π-back-bond and also on the Au-C-O angle. The soft bending potential may cause the structure optimization to deviate more strongly for slightly different conditions such as the choice of basis sets or initial structures.

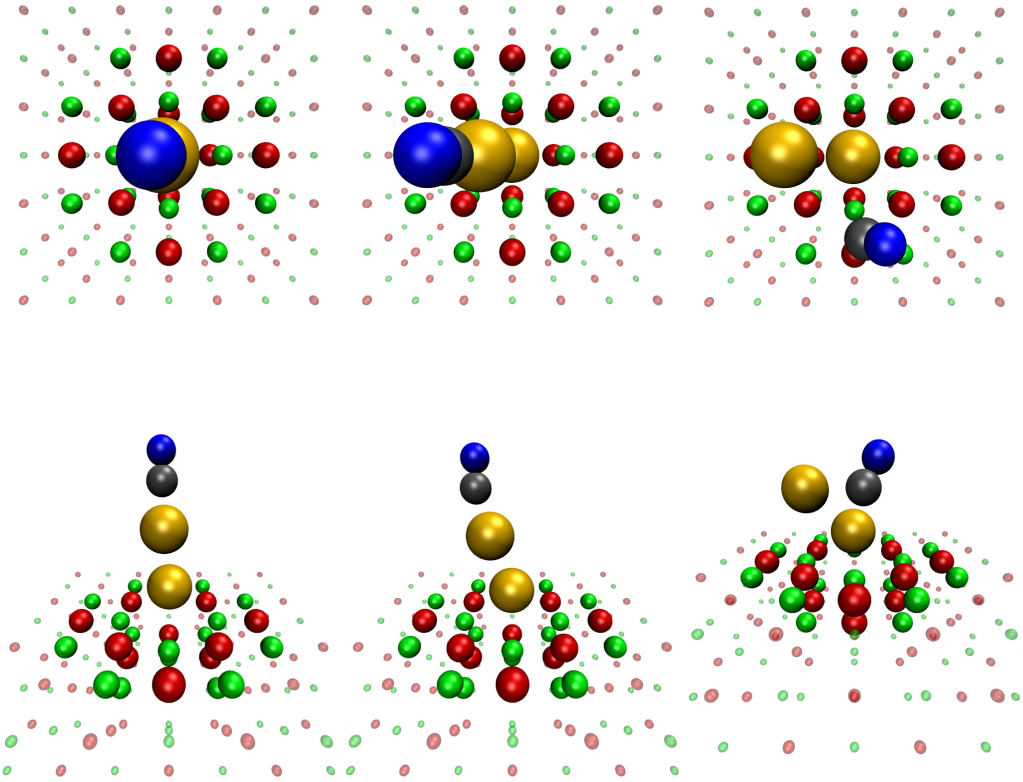

(a) Au_2CO/F^{2+}-MgO(001) **(b)** Au_2CO/F^{1+}-MgO(001) **(c)** Au_2CO/F^{0}-MgO(001)

Figure 5: Optimized structure for the adsorption of CO on different charged Au_2/F^{i+}-MgO(001) surfaces. The upper row shows the systems from above and the bottom row from the side. Colors are as in figure 4 and the O atom of the CO adsorbate is colored blue for clarity, whereas C is colored dark gray.

Table 4: Adsorption energy, vibrational frequency and C-O bond length of Au_2-CO/F^{2+}-MgO(001) from this work and literature values from Pacchioni et al.

system	Au_2-CO/F^{2+}-MgO(001)	
	this work	Pacchioni et al.
E_{ads}(Au-CO) in eV	1.39	1.18
ν(CO) in cm^{-1}	2203	2208
r(C-O) in Å	1.121	1.125

Compared to our results, the results from Pacchioni et al. [88] about the adsorption energy, vibrational frequency and C-O bond length of Au_2-CO/F^{2+}-MgO(001) are shown in table 4. The C-O stretch frequencies of Au_2-CO/F^{2+}-MgO(001) (2203 cm^{-1}) matches well with the literature value from Pacchioni et al. (2208 cm^{-1}). Furthermore the C-O bond length of 1.121 Å is is also in a good agreement with the literature value of 1.125 Å, but the adsorption energy of about 1.39 eV differs markedly from that of Pacchioni et al of 1.18 eV. Considering the large number of differences between both theoretical works (in particular effective core potentials, basis sets, embedding parameters ...) the choice of the systems gives satisfactory results and will be taken for the further calculations.

Table 5: Adsorption energies and structural parameters of the different charged $[Au_2CO]^n$. Adsorption energies are counterpoise corrected and a scaling factor of 0.970 has been applied to the computed frequencies [80].

system	$[Au_2CO]^+$	Au_2CO	$[Au_2CO]^-$
E_{ads}(Au-CO) in eV	1.50	0.98	0.38
ν(CO) in cm^{-1}	2216	2129	1787
r(Au-C) in Å	1.978	1.967	2.107
r(C-O) in Å	1.120	1.130	1.172
∠Au-C-O in [°]	179.5	178.6	129.5

The comparison of molecular parameters between different charged $[Au_2CO]$ systems in the gas phase and the supported Au_2-CO/F^{i+}-MgO(001) systems helps to evaluate the influence of the underlying defective MgO(001) surface. In table 5 are listed the adsorption energies, C-O stretch frequency and structural parameters of the neutral, positively and negatively charged $[Au_2CO]$ systems. The comparison between the various systems is reported in figure 6. These parameters have a similar dependence on the electric charge as the supported systems. For example the angle Au-C-O deviates more strongly from 180° with additional electrons contributing to the increased π-back-bond via the Au 6s orbital to the CO π^* orbitals, which only exists for non-linear conformation because of the symmetry of the orbitals. Also the C-O bond lengths increase with stronger π-back-donation because the anti-bonding CO π^* orbitals get occupied by electrons.

The comparison between the supported and the gas phase system shows, that the Au_2-CO /F^{2+}-MgO(001) system is in a good agreement with the positively charged $[Au_2CO]^+$. It appears that the F^{2+} vacancy pulls electron density from the gold cluster away. The neutral Au_2CO and Au_2-CO/F^{1+}-MgO(001) have similar values for ν(CO) and the C-O distance. This indicate a similar strength of the π-back-bond although the Au-C-O angle cannot quite compare. Note that this angle is crucial for the overlap of the orbitals and the strength of the π-back-bond. The equilibrium system of Au_2CO/F^0-MgO(001) is not easy to compare with the gas phase systems because of the different adsorption structures.

In figure 6, we report the Mulliken population analysis for all systems. The Mulliken charge of the CO adsorbed Au_2 cluster on the different charged defective MgO(001) surfaces is more negative than the gas phase systems with the same total charge. Especially the gold atoms pull electron density from MgO and that lead to about one more electronic charge for each gold atom. The higher negative charge of the gold cluster induces a stronger polarization in the CO, while the system with the F^0 vacancy departs from this trend but its adsorption behavior differs from the other cases and so the results must be treated carefully.

4.2.2 Adsorption of CO on Au_1/F^{i+}-MgO(001)

The adsorption energies and further structural parameters for the different charged systems are listed in table 6 and figure 7 shows the different charged systems. In contrast to the supported Au_2 cluster is the adsorption CO on one supported Au atom less strong.

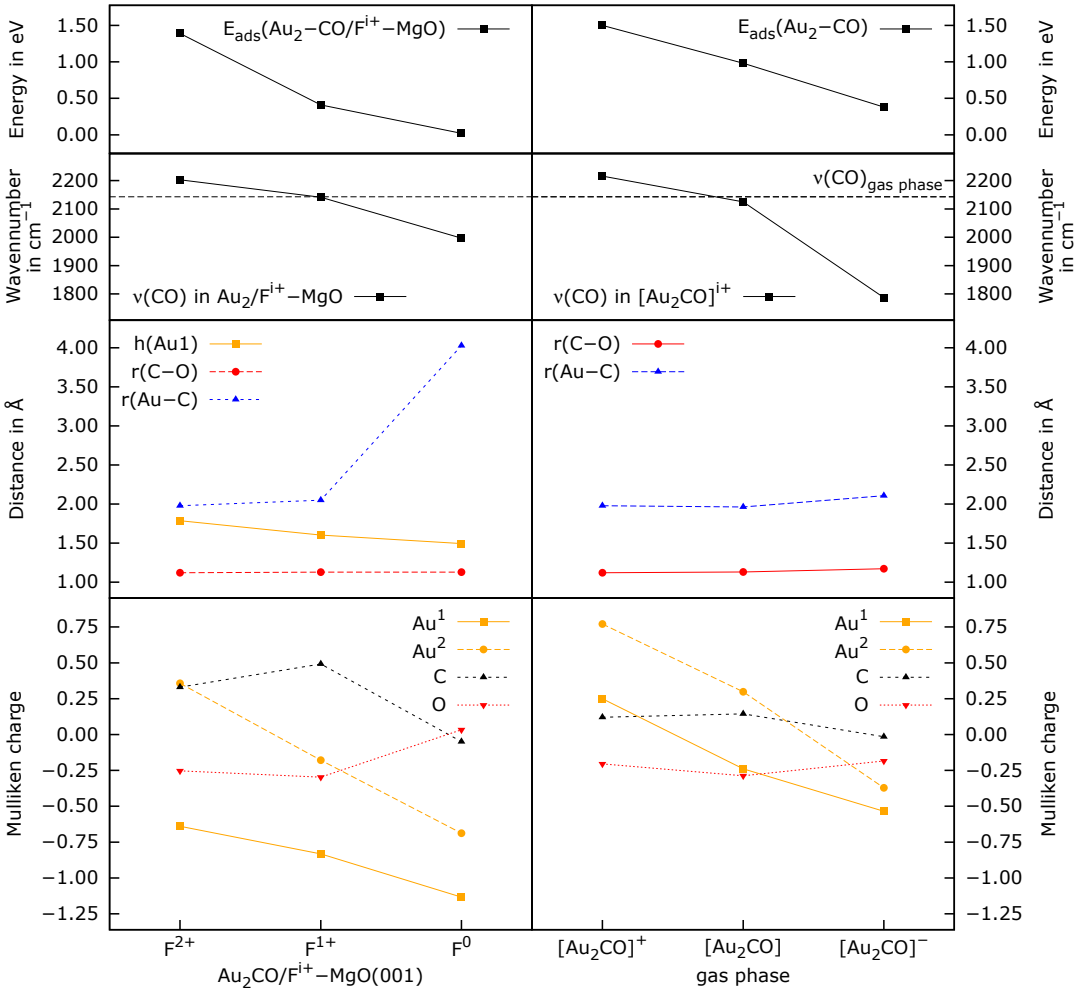

Figure 6: Comparison of adsorption energies (top panels), vibrational frequencies (second top panels), selected interatomic distances (third top panels) and Mulliken charges (bottom panels) of the CO adsorbed Au_2 cluster deposited on different charged defective MgO(001) surface (left column) with different charged gas phase systems (right column)

The adsorption energy of CO on Au_1/F^{2+}-MgO(001) with 0.52 eV is less than half as in the Au_2/F^{2+}-MgO(001) case. The reason for this may be the different chemical environment between a single supported Au atom a the upper gold atom in a supported Au_2 cluster, especially in the coordination number. The trend of a lower adsorption energy of CO on supported Au_1 as on Au_2 can also be seen for the lower charged vacancies. The most stable adsorption states for the Au_1-CO/F^{1+}-MgO(001) and the Au_1CO/F^0-MgO(001) systems are also not found on top of the gold atom but on the MgO surface next to the gold. Note that the used DFT-D3 dispersion correction used supports the adsorption behavior because of the increased coordination number of the adsorbate CO. A further difference is, that the adsorption energy of CO on Au_1/F^{1+}-MgO(001) is smaller (0.22 eV) then the adsorption energy of CO on Au_1/F^0-MgO(001) (0.39 eV). The weaker interaction between CO and gold in both systems is also represented by the different Au-C distances.

Table 6: Adsorption energies and structural parameters of the different charged Au_1-CO/F^{i+}-MgO(001). Adsorption energies are counterpoise corrected and a scaling factor of 0.970 has been applied to the computed frequencies [80].

system / Au_1-CO on	F^{2+}-MgO(001)	F^{1+}-MgO(001)	F^0-MgO(001)
adsorption behavior	atop	side	side
E_{ads}(Au-CO) in eV	0.52	0.22	0.39
ν(CO) in cm^{-1}	2206	2139	1811
r(Au-C) in Å	2.180	3.490	2.463
r(C-O) in Å	1.119	1.127	1.159
∠Au-C-O in [°]	179.1	122.1	139.6
r(Mg_{slab}-C) in Å	-	3.506	2.544

The C-O stretch frequency of the adsorbed carbon monoxide does also strongly depend on the charge of the supported gold atom. The electron poor Au_1-CO/F^{2+}-MgO(001) system shows no or a very weak π-back-bond, what leads to a blue shift of the C-O stretch frequency by +60 cm^{-1} in comparison to CO in the gas phase to 2206 cm^{-1} (see fig. 8). The nearly linear conformation of Au-C-O supports this observation, because the π-back-bond from Au 6s to the CO π^* orbital cannot exist in a linear conformation. Like in Au_2-CO/F^{2+}-MgO(001) the blue shift is induced by the stepper potential for the bonding elongation of the C-O bond length caused by the adsorption on gold. In the Au_1CO/F^{1+}-MgO(001) system CO adsorbs on the MgO surface next to the gold atom and the C-O stretch frequency of 2139 cm^{-1} is nearly the same like CO in the gas phase with 2143 cm^{-1}. This result is as for the Au_2 cluster on F^{1+}-MgO(001) but here the Au-C distance of 3.490 Å prevents a stronger π-back-bond. The Au-C distance is in a good agreement with the sum of the van der Waals radii of C (1.77 Å) and Au (1.60 Å) of 3.36 Å. This support the hypothesis of interaction between both atoms dominated by weak van-der-Waals interaction/London forces. The C-O stretch frequency in the Au_1CO/F^0-MgO(001) system is red shifted by -332 cm^{-1}. This is a result of the π-back-bond from the electron saturated system to the anti-bonding π^* orbitals, which is shown by an increased C-O distance from 1.128 Å in the gas phase to 1.159 Å. The π-back-bond proceeds from the MgO(001) surface and maybe from the gold atom even so the Au-C distance of 2.463 Å is much higher than the sum of both covalent radii. The Au-C-O bonding angle of 139.6° is depends not only on the π-back-donation from the gold atom but also on the π-back-donation from the Mg ion of the surface.

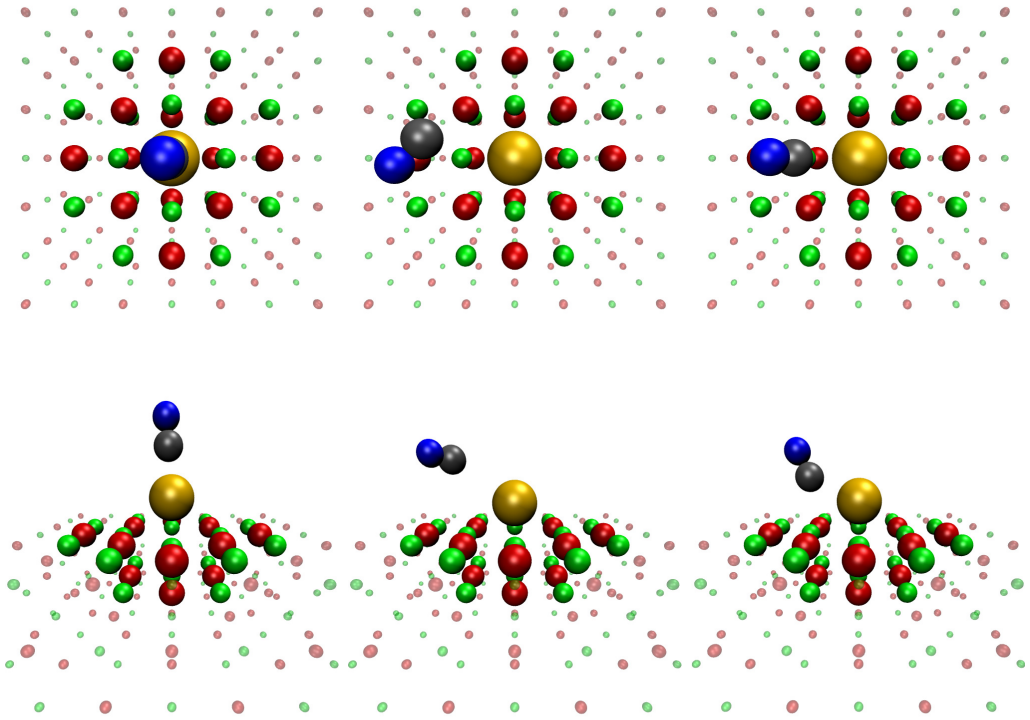

(a) Au_1CO/F^{2+}-MgO(001) **(b)** Au_1CO/F^{1+}-MgO(001) **(c)** Au_1CO/F^{0}-MgO(001)

Figure 7: Optimized structures for the different charged Au_1CO/F^{i+}-MgO(001) systems. The upper row shows the systems from above and the bottom row from the side. The O atom of the CO adsorbate is colored blue for clarity, whereas C is colored dark gray..

Table 7: Adsorption energy, vibrational frequency and C-O bond length of Au_1-CO/F^{2+}-MgO(001) from this work and literature values from Pacchioni et al.

system	Au_1-CO/F^{2+}-MgO(001)	
	this work	Pacchioni et al.
E_{ads}(Au-CO) in eV	0.52	0.21
ν(CO) in cm^{-1}	2206	2207
r(C-O) in Å	1.119	1.123

Compared to our results, the results from Pacchioni et al. [88] about the adsorption energy, vibrational frequency and C-O bond length of Au_1-CO/F^{2+}-MgO(001) are shown in table 7. The vibrational stretch frequency of CO (2207 cm^{-1}) and the C-O bond length (1.123 Å) from are Pacchioni et al. are in good agreement to our values. The deviation of the adsorption energy of Pacchioni et al. (0.21 eV) from our calculated adsorption energy (0.52 eV) of CO on Au_1/F^{2+}-MgO(001) is even larger than in the Au_2-CO/F^{2+}-MgO(001) system. Considering besides the differences between both systems (effective core potential, basis sets, embedding parameters ...) and the additional DFT-D3 correction in our calculation the deviation of the adsorption energies corresponds to the deviation in the Au_2-CO/F^{2+}-MgO(001) system.

Table 8: Adsorption energies and structural parameters of the different charged $[Au_1CO]^n$. Adsorption energies are counterpoise corrected and a scaling factor of 0.970 has been applied to the computed frequencies [80].

system	$[Au_1CO]^+$	Au_1CO	$[Au_1CO]^-$
E_{ads}(Au-CO) in eV	2.01	0.33	0.17
ν(CO) in cm^{-1}	2242	2003	1943
r(Au-C) in Å	1.948	2.097	2.689
r(C-O) in Å	1.117	1.141	1.150
∠Au-C-O in [°]	180.0	137.7	112.0

As in the previous chapter the comparison of the supported system with different charged $[Au_1CO]$ cluster in the gas phase helps us again to evaluate the influence of the defective MgO(001) surface. In table 12 are listed the adsorption energies, C-O stretch frequency and structural parameters of the neutral, positively and negatively charged $[Au_1CO]$ system. Because of the different adsorption behavior for the Au_1 cluster deposited on F^{1+}-MgO(001) and F^0-MgO(001) the comparison has to be treated carefully. One of the biggest deviation is the high adsorption energy of CO on a single positive charged gold ion of 2.01 eV. The neutral and negatively charged gas phase systems have similar adsorption energies as the supported systems. The C-O stretch frequency for adsorbed CO in $[Au_1CO]^+$ is shifted to a higher wavenumber by $+98$ cm^{-1} compared to the free CO because of the missing π-back-bond, which is also indicated by the linear conformation. In contrast to Au_2CO the C-O stretch frequency of Au_1CO is already red shifted by -140 cm^{-1} accompanied with a stretched C-O distance and a smaller Au-C-O angle. This trend continuous for $[Au_1CO]^-$.

In figure 8 are listed the different parameters of the supported and the gas phase systems. A look at the Mulliken charges reveals again a polarization of the adsorbed CO atop on the gold atom deposited on the F^{2+}-MgO(001) surface. In the case of an adsorption next to the gold atom like in the other cases there is no strong polarization observable. However the gold atom pulls once more electron density from the MgO(001) surface. For the supported systems with a total charge of +1 the Mulliken charge for the Au atom in the supported system is -2.395 e^- more negatively charged than $[Au_1CO]^+$ in the gas phase. Even the Au_1CO/F^{2+}-MgO(001) system has a negatively charged Au atom than $[Au_1CO]^+$ (-1.760 e^- vs. 1.165 e^-) which may causes the deviation in the adsorption energies. For the supported Au_2 cluster the top Au atom has a smaller deviation from the Au atoms in the gas phase systems. The Mulliken charge of the Au atom in the neutral and negatively charged gas phase systems falls to negative values resulting in similar CO adsorption energies as in the supported systems.

4.2.3 Adsorption of O_2 on Au_2/F^{i+}-MgO(001)

The adsorption of molecular oxygen on Au_2/F^{i+}-MgO(001) is difficult to handle, because the adsorption energy are lower than for the CO adsorbent. Therefore it is necessary to include dispersion correction to get an improved description for the possible physisorption. Calculations show no stable adsorption state without the enabled dispersion correction

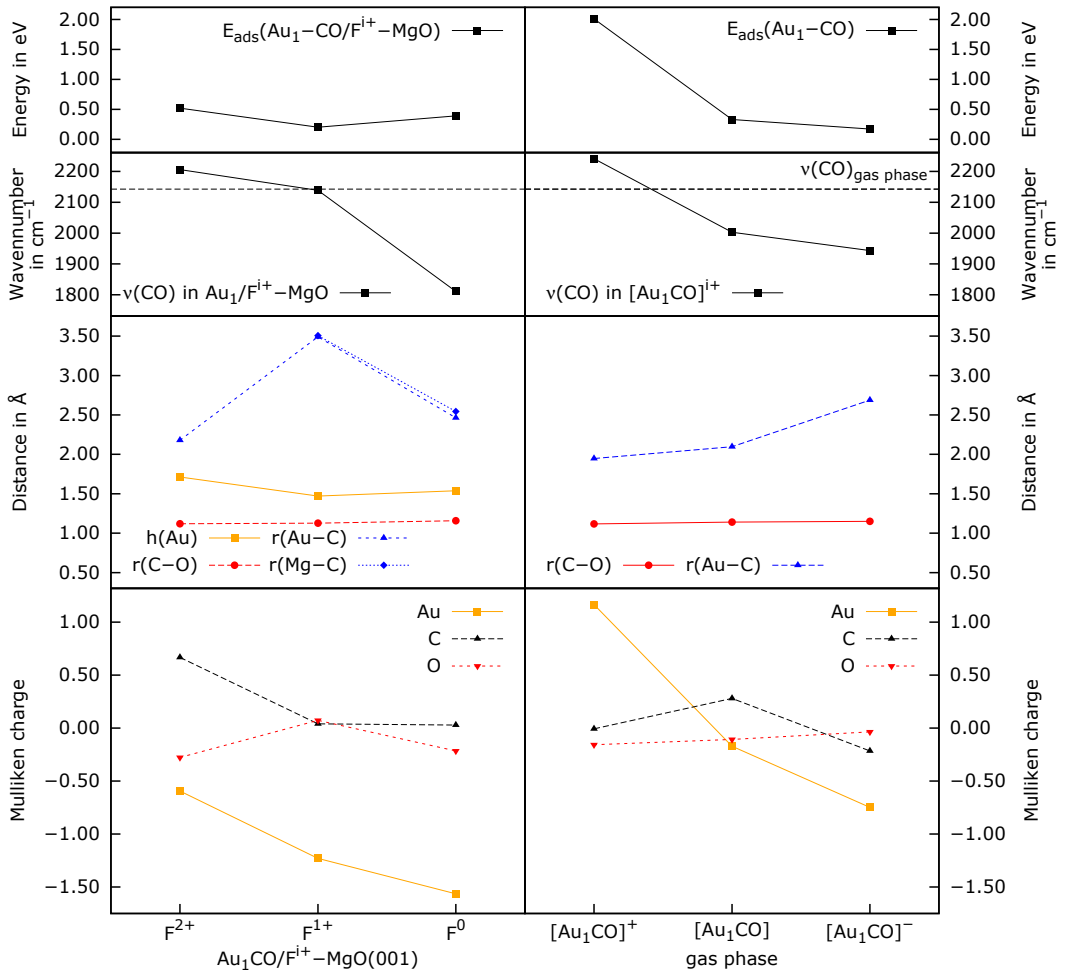

Figure 8: Comparison of adsorption energies (top panels), vibrational frequencies (second top), selected interatomic distances (third top panels) and Mulliken charges (bottom panels) of the CO adsorbed Au_1 cluster deposited on different charged defective MgO(001) surface (left column) with different charged gas phase systems (right column)

for Au_2-O_2/F^0-MgO(001). However, including the DFT-D3 dispersion correction in the DFT calculation leads to a lateral displacement and eventually to the diffusion of the upper Au atom. The result of structure optimization can therefore be rationalized in terms of a single Au atom filling the vacancy and the second Au atom with molecular oxygen adsorbed on top bounded on an oxygen ion of the MgO(001) surface.

Without DFT-D3 dispersion correction one finds a very small adsorption energy for O_2 on Au_2/F^{1+}-MgO(001) of 0.12 eV. This may a consequence of the spin contamination, because the energetically favorable doublet state is contaminated with the energetic higher quartet state resulting in a higher total energy and lowers the adsorption energy. The Au_2-O_2/F^{2+}-MgO(001) system is different. Here, the high spin triplet state is energetically more favorable and shows no spin contamination like the low spin singlet state, that results in the reliable adsorption energy of 0.47 eV. In contrast to CO as adsorbate, the

Au_2 cluster tilt to the surface as it is shown in figure 9. The O_2 stretch frequency exhibits a red shift in the Au_2O_2/F^{2+}-MgO(001) system by -28 cm^{-1}. This is rather caused by a π-back-donation from the MgO(001) surface to O_2. With an additional electron the red shift of the O_2 stretch frequency increases to -217 cm^{-1} and so the O-O bond distance do because of the occupation of the anti-bonding π^* orbitals. The structure optimization of Au_2O_2/F^0-MgO(001) results in unreliable structures with dissociated O atoms somewhere in the gas phase. Surely further investigation will lead to proper structures but probably with a high spin contamination as well. Due to the highly irregular absorption behavior of this system, it was put aside in the remaining investigations.

Table 9: Adsorption energies and structural parameters of the different charged Au_2-O_2/F^{i+}-MgO(001). Adsorption energies are counterpoise corrected and a scaling factor of 0.970 has been applied to the computed frequencies [80].

system / Au_2-O_2 on	F^{2+}-MgO(001)	F^{1+}-MgO(001)
E_{ads}(Au-O_2) in eV	0.47	0.12
$\nu(O_2)$ in cm^{-1}	1562	1363
r(Au-O) in Å	2.645	2.330
r(O-O) in Å	1.206	1.230
∠Au-C-O in [°]	127.3	121.0
$\langle S^2 \rangle$	2.00	1.35

Figure 10 shows the spin density of the Au_2/F^{2+}-MgO(001) in the pure triplet state and the spin contaminated doublet state of Au_2/F^{1+}-MgO(001). It is observed that the physisorption of O_2 leads to highly spin contaminated results if the low spin state is favorable in energy but still near the high spin state. In the case of Au_2/F^{2+}-MgO(001) in the singlet state the system will be a mixture of the singlet and the triplet state, that is revealed by an $\langle S^2 \rangle$ expectation value of 1.00. Due to the same spin state of the unpaired electron in the triplet state there is no mixing and the $\langle S^2 \rangle$ expectation value corresponds to the theoretical value of $\langle S^2 \rangle_{triplet} = 2.00$. The results of the Au_2/F^{1+}-MgO(001) system are spin contaminated with an $\langle S^2 \rangle$ expectation value of 1.35 between that of a doublet $\langle S^2 \rangle_{doublet} = 0.75$ and a quartet state $\langle S^2 \rangle_{quartet} = 3.75$. It shows that the results about the Au_2-O_2/F^{1+}-MgO(001) system are not reliable by using a single determinant ansatz due to strong multi reference effects.

Table 10 contains the adsorption energies, vibrational frequencies and structural parameters of different charged $[Au_2O_2]$ clusters in the gas phase. Despite the short Au-O distances the O_2 molecule is only weakly bound in the positively and neutral charged system with adsorption energies of 0.15 eV and 0.05 eV, respectively. It shows that the energetically more stable electronic states are with a triplet state for the O_2 adsorbate and either the doublet state for the single positive charged system, which gives in combination a quartet state, or a singlet state for the neutral charged system resulting in a combined triplet state. The weak interaction is also indicated by the small red shift of the vibrational O-O stretch frequencies with -29 cm^{-1} and -60 cm^{-1} for the positively and neutral charged cluster, respectively. The stronger red shift in the neutral charged system is caused by the better π-back-donation from the Au atom, which is indicated by the smaller Au-O-O angle of 122.7°, but the longer Au-O distance does slightly compensate this π-back-bond. Only the negatively charged system shows a strong interaction between the Au_2 cluster and O_2. As a result this system has the largest adsorption energy

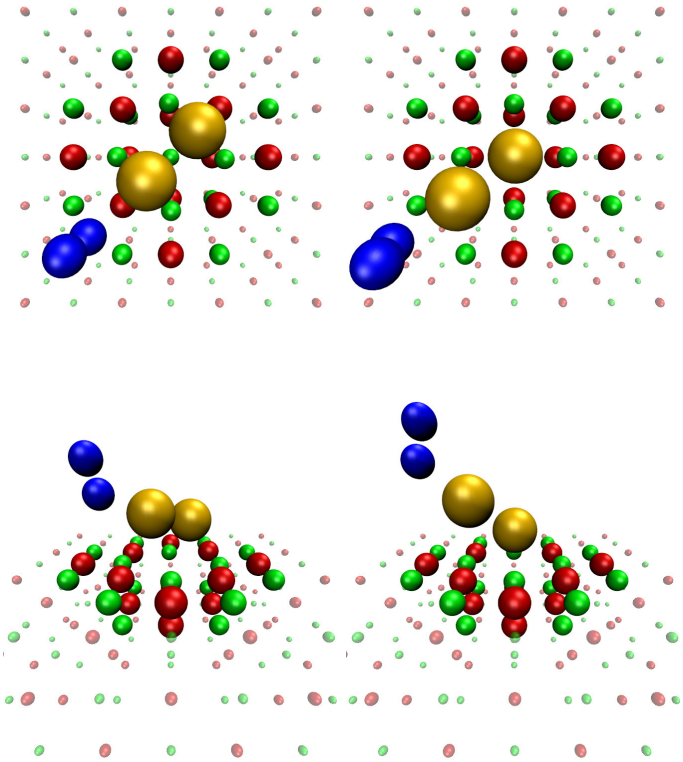

(a) Au_2O_2/F^{2+}-MgO(001) **(b)** Au_2O_2/F^{1+}-MgO(001)

Figure 9: Optimized structures for the different charged Au_2O_2/F^{i+}-MgO(001) systems. The upper row shows the systems from above and the bottom row from the side. The O_2 adsorbate is colored blue for clarity.

with 0.93 eV and is also more stable in the electronic doublet state as compared with the quartet state as in $[Au_2Au_2]^+$. The electron rich system does also have the strongest π-back-bond which is indicated by the short Au-O bond distance with 2.161 Å and the small Au-O-O angle with 117.0°. This lead to a red shift of the vibrational O-O stretch frequency of -445 cm^{-1}.

Table 10: Adsorption energies and structural parameters of the different charged $[Au_2O_2]^n$. Adsorption energies are counterpoise corrected and a scaling factor of 0.970 has been applied to the computed frequencies [80].

system	$[Au_2O_2]^+$	Au_2O_2	$[Au_2O_2]^-$
E_{ads}(Au-Au_2) in eV	0.15	0.05	0.93
ν(Au_2) in cm^{-1}	1551	1520	1135
r(Au-O) in Å	2.376	2.478	2.161
r(O-O) in Å	1.204	1.211	1.310
∠Au-O-O in [°]	174.8	122.7	117.0
$\langle S^2 \rangle$	3.77	2.01	0.77

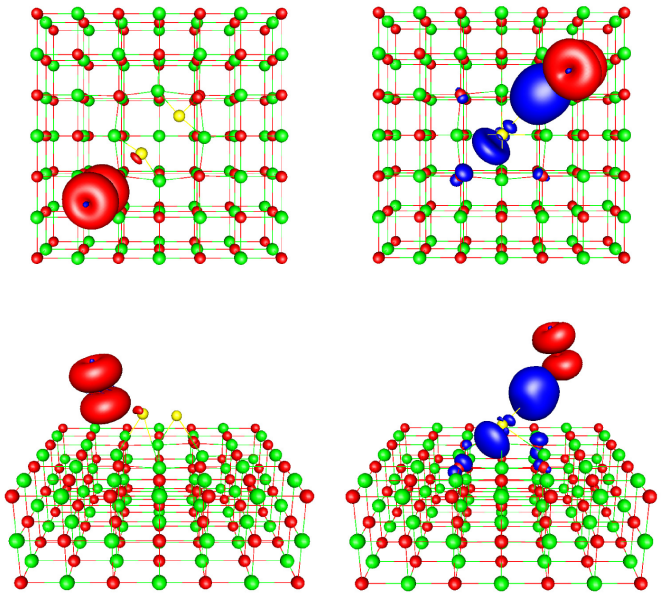

(a) Au_2O_2/F^{2+}-MgO(001) $\langle S^2 \rangle = 2.00$ **(b)** Au_2O_2/F^{1+}-MgO(001) $\langle S^2 \rangle = 1.35$

Figure 10: Spin density map of the two different charged Au_2O_2/F^{i+}-MgO(001) systems. The upper row shows the systems from above and the bottom row from the side. The spin density boundaries are shown at ± 0.002. (a) Au_1O_2/F^{2+}-MgO(001) is in a pure triplet state, which is energetically more favorable than the spin contaminated singulet state. In (b) is shown the spin density of Au_1O_2/F^{1+}-MgO(001) in the spin contaminated doublet state.

4.2.4 Adsorption of O_2 on Au_1/F^{i+}-MgO(001)

The adsorption of O_2 on a single Au atom deposited on the defective MgO(001) surface leads to interesting results on which one has to take a closer look. Firstly O_2 does not adsorb atop on the Au atom in any of the different charged systems. In the Au_1/F^{2+}-MgO(001) and Au_1/F^{1+}-MgO(001) system O_2 adsorbs preferentially next to the Au atom on the MgO(001) surface with adsorption energies of 0.17 eV and 0.20 eV, respectively. Experiments shown that the adsorption energy of O_2 on a clean MgO(001) surface is 0.14 eV [93] and DFT calculations result in an adsorption value of 0.16 eV [94]. That agrees on the calculated values, which are also influenced by the dispersion interaction to the Au atom. A special case is the Au_1O_2/F^0-MgO(001) system, where O_2 forms a bridge from a Mg ion to the Au atom which is shown in figure 11. This conformation leads to a high adsorption energy of 1.81 eV and this conformation is not observed on the two other charged systems.

As we have seen in the previous chapter results of systems with adsorbed O_2 can be spin contaminated and unreliable. Here, Au_1O_2/F^{2+}-MgO(001) has a $\langle S^2 \rangle$ expectation value of 1.71, which indicates a mixed state with doublet and quartet character. This spin contamination is an effect of the physisorption of an adsorbate in a triplet state (O_2) on deposited Au atom in a doublet state (Au_1/F^{2+}-MgO(001)). For the Au_1O_2/F^{1+}-

Table 11: Adsorption energies and structural parameters of the different charged Au_2-O_2/F^{i+}-MgO(001). Adsorption energies are counterpoise corrected and a scaling factor of 0.970 has been applied to the computed frequencies [80].

system / Au_1-O_2 on	F^{2+}-MgO(001)	F^{1+}-MgO(001)	F^{0}-MgO(001)
E_{ads}(Au-O_2) in eV	0.17	0.20	1.81
$\nu(O_2)$ in cm^{-1}	1561	1577	1149
r(Au-O) in Å	2.951	3.397	2.450
r(O-O) in Å	1.205	1.206	1.330
∠Au-O-O in [°]	125.0	123.1	94.7
$\langle S^2 \rangle$	1.71	2.00	0.76

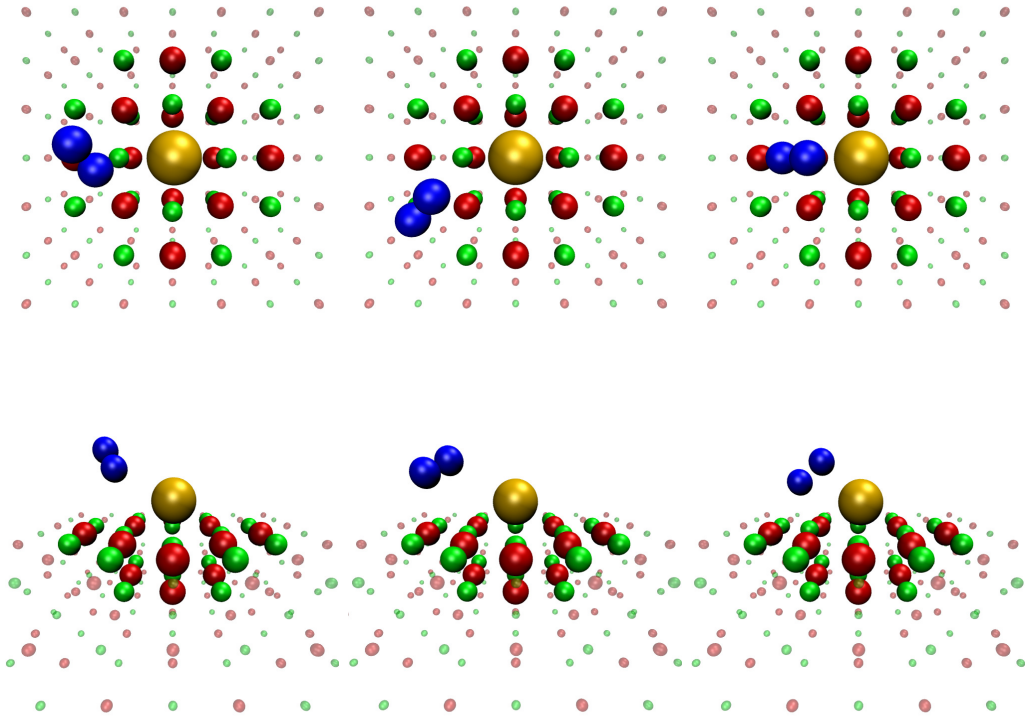

(a) Au_1O_2/F^{2+}-MgO(001) **(b)** Au_1O_2/F^{1+}-MgO(001) **(c)** Au_1O_2/F^{0}-MgO(001)

Figure 11: Optimized structures for the different charged Au_1O_2/F^{i+}-MgO(001) systems. The upper row shows the systems from above and the bottom row from the side. The O_2 adsorbate is colored blue for clarity.

MgO(001) system the additional electron is found on the Au atom which remains in a singlet state and therefore the spin contamination vanishes even though O_2 is only physisorbed. The spin contamination does also vanish if O_2 adsorbs chemically and induce a stronger electronic correlation between O_2 and the Au atom as in the case of Au_1O_2/F^0-MgO(001). The spin density maps in figure 12 does also support this hypothesis. In figure 12a O_2 with two unpaired α-electrons is contaminated by β-electron density of the Au and the wave function is contaminated by a high spin quartet state. In figure 12c the contribution of the quartet state nearly vanished because one of the

two unpaired electrons of O_2 pairs with the unpaired electron of the F^0 surface system. Hence, the doublet state dominates, with an unpaired electron density located in the π^* orbitals of O_2. Investigation of reaction paths for the catalytic oxidation on the Au_1/F^{2+}-MgO(001) system shows that the spin contamination also vanish if O_2 comes from its physical adsorbed state into a stronger interaction with the surface system, as seen for Au_1O_2/F^0-MgO(001). Furthermore, if two more electrons are added to the Au_1O_2/F^{2+}-MgO(001) system ($F^{2+} \rightarrow F^0$ with the conformation of Au_1O_2/F^{2+}-MgO(001)), the spin contamination is lowered to 1.00 but it is still remarkable. Figure 12b shows that in the case of one additional electron the Au atom change into a singlet state and the α-electron density is only located on O_2. One way to prevent spin contamination in the calculation of the Au_1O_2/F^{2+}-MgO(001) system is to force a quartet state but this state is about 0.036 eV higher in energy than the spin contaminated system. A second way to minimize spin contamination is by using a smaller basis set to avoid a deviation between the spatial orbitals of the α- and β-electrons. Since our calculations are already done with a relatively small basis set, this approach would yield completely unreliable results.

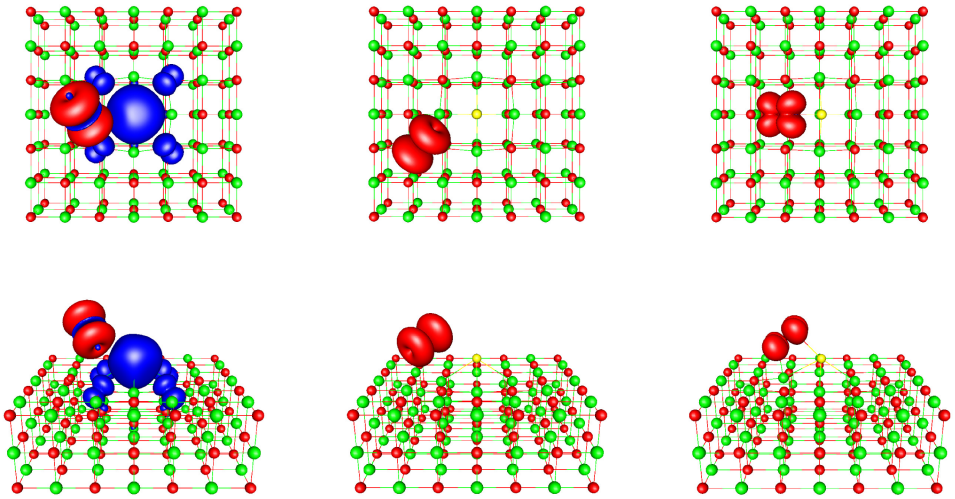

(a) Au_1O_2/F^{2+}-MgO(001) $\langle S^2 \rangle = 1.71$ **(b)** Au_1O_2/F^{1+}-MgO(001) $\langle S^2 \rangle = 2.00$ **(c)** Au_1O_2/F^0-MgO(001) $\langle S^2 \rangle = 0.76$

Figure 12: Spin density map of the different charged Au_1O_2/F^{i+}-MgO(001) systems. The upper row shows the systems from above and the bottom row from the side. The spin density boundaries are shown at ± 0.002. (a) Au_1O_2/F^{2+}-MgO(001) shows a doublet state, which is spin contaminated by a quartet state, where the two unpaired electrons of O_2 and the single unpaired electron of the Au atom have the same electron spin. The additional electron in (b) Au_1O_2/F^{1+}-MgO(001) forms a singlet state on Au_1/F^{1+}-MgO(001) and O_2 remains in a pure triplet state. The doublet state of (c) Au_1O_2/F^0-MgO(001) is not a result of the two additional electrons, but a result of the stronger interaction between the O_2 adsorbate and the supported Au atom. If two electrons are added to the conformation of (a) $Au_1O_2/F^{2+ \rightarrow 0}$-MgO(001) the spin contamination does only lowers to a $\langle S^2 \rangle$ expectation value of 1.00.

A look at the vibrational O-O stretch frequency shows for Au_1O_2/F^{2+}-MgO(001) and Au_1O_2/F^{1+}-MgO(001) only a small red shift by -19 cm^{-1} and -3 cm^{-1}, respectively ($\nu(O_{2,\text{gas phase}}) = 1580\text{cm}^{-1}$). Interestingly the O-O stretch frequency in the F^{2+} system shows a stronger red shift than in the F^{1+} system, even though the F^{1+} system is less

electron poor and can more easily donate electrons into the anti-bonding π^* orbitals. This observation results from the larger Au-O distance of the F^{1+} system than in the F^{2+} system or the spin contamination effect unreliable results for the vibrational frequencies as well. In Au_1O_2/F^0-MgO(001) the O-O stretch frequency is strongly red shifted by -431 cm^{-1}. This strong red shift is also shown in a strongly increased O-O bond distance by +0.122 Å as compared to the O-O bond distance of free O_2 (1.208 Å). This strong increase of the O-O bond length lowers the remaining energy for the dissociation of the O-O bond, which is an important step towards a catalytic oxidation of CO with O_2.

Table 12: Adsorption energies and structural parameters of the different charged $[Au_1O_2]^n$. Adsorption energies are counterpoise corrected and a scaling factor of 0.970 has been applied to the computed frequencies [80].

system	$[Au_1O_2]^+$	Au_1O_2	$[Au_1O_2]^-$
E_{ads}(Au-O_2) in eV	0.48	0.07	0.31
ν(O-O) in cm^{-1}	1530	1526	1306
r(Au-O) in Å	2.366	2.734	2.967
r(O-O) in Å	1.203	1.208	1.244
∠Au-O-O in [°]	124.6	118.8	121.4
$\langle S^2 \rangle$	2.01	1.66	2.01

A compilation of the results of the Au_1O_2 systems in the gas phase are shown in table 12. The Au_1O_2 cluster in the gas phase shows also a small adsorption energy for the neutral charged systems of 0.07 eV. This value matches with a benchmark calculation from Fang et al. [95], but B3LYP overestimates the adsorption energy compared to a MRCI (multireference correlation interaction) calculation with a value of 0.02 eV. Furthermore the Au-O bond length of 2.734 Å differs strongly from the result of Fang et al. (2.197 Å) using the B3LYP functional with an augmented correlation-corrected quadruple-zeta basis set (aug-cc-pQDZ), whereas structure optimization at the MRCI level predicts a Au-O distance of 3.584 Å. The difference between the two results of the B3LYP calculations are not caused by the DFT-D3 correction, because calculation without dispersion correction results in a Au-O distance of 2.537 Åbut with the same adsorption energy of 0.07 eV. Calculations with the same aug-cc-pVQZ basis set used by Fang et al. [95] leads to similar results. The Au-O bond length is shortened to 2.239 Åwith an adsorption energy of 0.08 eV. The remaining deviations may comes from the different electron core potential for the Au atom. Also the results of the neutral charged Au_1O_2 cluster are spin contaminated and therefore unreliable as well. In general Fang et al. [95] mentioned that the weak interaction between Au and O_2 is the source of difficulties in both experiments and theoretical calculations and concludes that long range corrected functionals show a good overall performance. As an example for the difficulties for theoretical calculations in the paper of Metiu et al. [96] Au_1O_2 and $[Au_1O_2]^-$ clusters are calculated with the PBE functional and projector augmented wave function, which results in adsorption values of 0.54 eV and 0.50 eV. Nevertheless the negatively charged $[Au_1O_2]^-$ cluster has an adsorption energy of 0.31 eV in a good agreement with the long Au-O distance of 2.967 Å. In the most electron rich Au_1O_2/F^0-MgO(001) system, the O-O bond length increases, but only by about +0.036 Å compared to O_2 in the gas phase. The strong adsorption energy of 1.81 eV cannot be reproduced in the gas phase system. Analogous to the single negative charged system, the positively charged $[Au_1O_2]^+$ has a stronger adsorption energy of 0.48 eV than the neutral system. Furthermore both

systems are in pure triplet state, but it is not able to explain the stronger deviation in the Au-O distance.

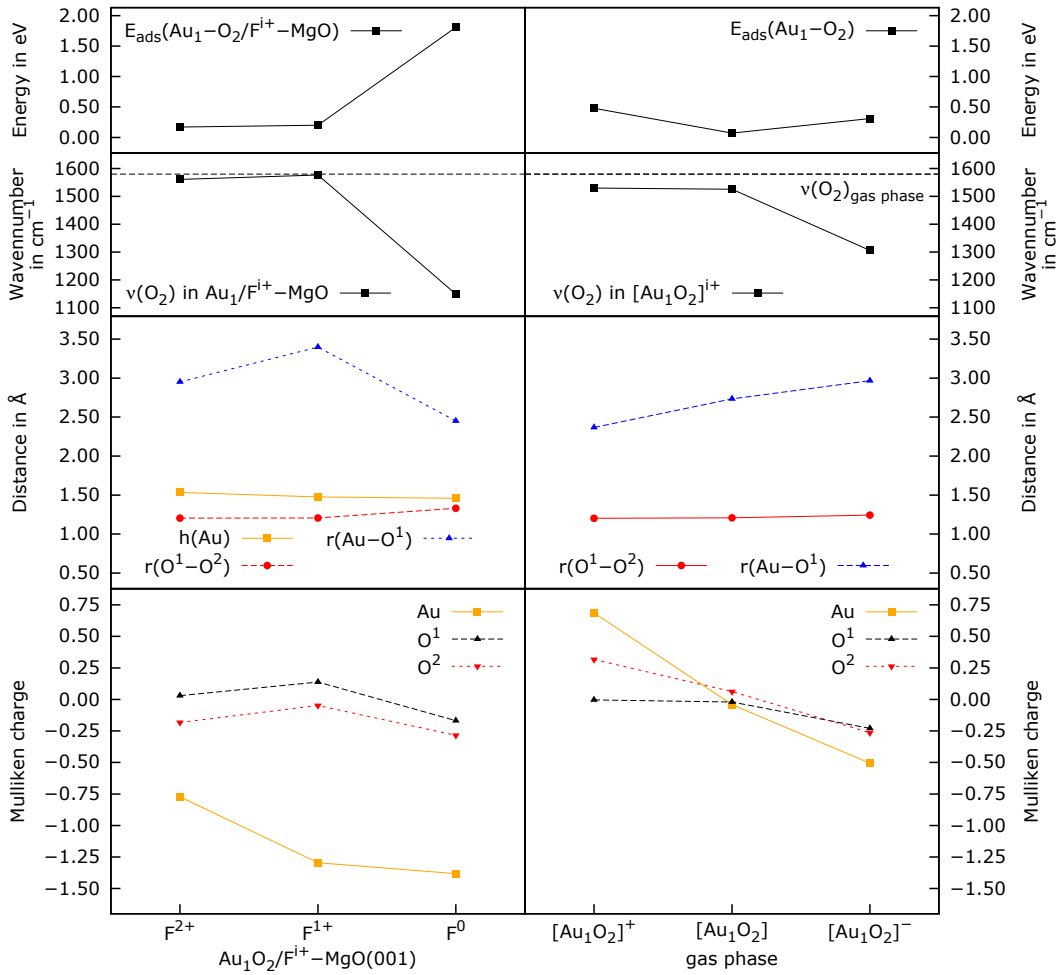

Figure 13: Comparison of adsorption energies, vibrational frequencies, structural parameters and Mulliken charges of the O_2 adsorbed Au_1 cluster deposited on different charged defective MgO(001) surface (left column) with different charged gas phase systems (right column)

Compared to the supported system the gas phase system shows a similar dependence of the Mulliken charge on the total charge of the system. The Mulliken charge of the Au atom decreases by adding electrons to the system but, in the supported system, the charge of the Au atom is strongly shifted to negative values relative to the gas phase systems. Actually, the different adsorption behavior of the supported systems compared to the gas phase systems make a direct comparison of catalytic cycles in the gas phase and on defective MgO(001) meaningless. In general it is shown clearly that the deposition of a single Au atom on a defective MgO(001) surface changes the chemical properties dramatically.

In conclusion, the investigation of either CO or O_2 on Au_1 and Au_2 atoms deposited on

defective MgO(001) surfaces leads to knowledge about possible initial structures for the catalytic oxidation of CO. However, the unreliable results for the adsorption of O_2 on Au_2/F^{i+}-MgO(001) complicate further investigations, and only the Au_1/F^{i+}-MgO(001) systems were studied here.

4.3 Catalytic oxidation of CO with O_2 on Au_1/F^{2+}-MgO(001)

In the following we investigate possible reaction paths for the catalytic oxidation of CO with O_2 on Au_1/F^{2+}-MgO(001). We start to get an initial structure with a co-adsorption of CO and O_2. The strongly exothermic reaction opens up many possible reaction channels with either adsorbed CO_2 on the Au cluster or desorbed CO_2. Further, an important question to be clarified is what happened to the remaining oxygen atom after the formation of the first CO_2.

4.3.1 Co-adsorption of CO and O_2 on Au_1/F^{2+}-MgO(001)

From the investigation of the single absorption of CO or O_2 on Au_1/F^{2+}-MgO(001) one can assume that a probable structure for the co-adsorption has a CO adsorbed atop on the Au cluster and a O_2 adsorbed next to the Au cluster on the MgO(001) surface. The structure optimization using this initial structure leads to the system in figure 14. In table 13 are listed the adsorption energies, vibrational frequencies and structural parameters of the co-adsorbed system compared to both single adsorbed systems.

Table 13: Adsorption energies, vibrational frequencies and structural parameters of single and co-adsorbed system of CO and/or O_2 on Au_1/F^{2+}-MgO(001). Adsorption energies are counterpoise corrected and a scaling factor of 0.970 has been applied to the computed frequencies [80]. In general the co-adsorbed system does not deviate large from the single adsorbed systems because of the different adsorption behavior of CO and O_2 on Au_1/F^{2+}-MgO(001).

system	Au_1-CO/F^{2+}-MgO(001)	Au_1-CO+O_2/F^{2+}-MgO(001)	Au_1-O_2/F^{2+}-MgO(001)
E_{ads}(Au-CO) in eV	0.53	0.47	-
ν(CO) in cm^{-1}	2206	2203	-
r(Au-C) in Å	2.180	2.183	-
r(C-O) in Å	1.119	1.119	-
∠Au-C-O in [°]	179.1	178.3	-
E_{ads}(Au-O_2) in eV	-	0.16	0.17
ν(O-O) in cm^{-1}	-	1558	1561
r(Au-O) in Å	-	3.243	2.951
r(O-O) in Å	-	1.205	1.205
∠Au-O-O in [°]	-	157.3	125.0
$\langle S^2 \rangle$	0.75	1.76	1.71

The counterpoise corrected adsorption energies shows a small decrease compared to the

single adsorbed systems of -0.05 eV for CO and -0.01 eV for O_2. It appears that CO does still preferably adsorbs atop on the Au cluster with an adsorption energy of 0.47 eV and O_2 is adsorbed next to the gold cluster with an adsorption energy of 0.16 eV. This particular geometry could be an artifact of our choice of the initial structure for the optimization. This slightly different adsorption behavior leads to little interaction between the two adsorbates, so the other structural parameters and the vibrational frequencies shows no large deviation from the single adsorbed systems. However the additional adsorbed CO on the Au cluster leads to a different optimal orientation of the O_2 adsorbate directly towards the CO adsorbed Au atom (compare top view of figure 11c and 14). In the singly adsorbed system the O-O bond is not orientated towards the gold cluster, but the additional interaction between O_2 and CO leads to the new preferred orientation of the O-O bond towards the cluster and to a larger distance from the central Au atom.

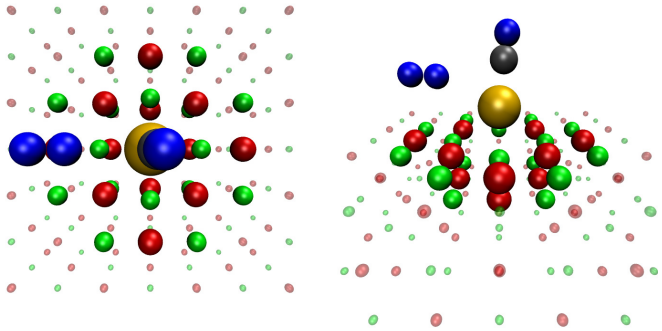

Figure 14: Optimized structure for the co-adsorption of CO and O_2 on Au_1/F^{2+}-MgO(001). The left panel shows a top view from the system and the right panel shows it from the side. The O atoms from the adsorbates are colored blue for a better overview, whereas C is colored dark gray. Except for the different orientation of the O_2 adsorbate the system shows no large deviation from a combination of the two single adsorbed systems.

The small adsorption energy of O_2 seems to indicate that a co-adsorption reaction would place between a precursor state with CO adsorbed on Au_1/F^{2+}-MgO(001) and O_2 either coming from the gas phase or diffusing on the MgO(001) surface. This picture is consistent with the high spin contamination observed at the co-adsorption minimum (see figure 15). Should a catalytic oxidation of CO occur on Au_1/F^{2+}-MgO(001) the calculated values for the reaction path would remain unreliable until a stronger interaction between the surface and O_2 leads to a pure doublet state. Note that, for this initial conformation, it is also possible to avoid the spin contamination by forcing the system in the quartet state, which is only about $+0.006$ eV higher in energy than the spin contaminated doublet state. The similar energy of both spin states can be explained by the larger distance of O_2 from the Au atom and the further delocalization of the unpaired electron from the Au atom over the adsorbed CO molecule. Hence, we will it should be keep an eye on the system in the electronic quartet state during the next investigations.

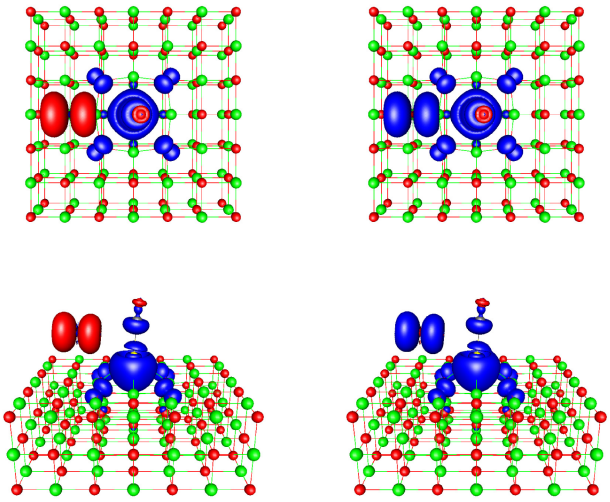

(a) doublet state: $\langle S^2 \rangle = 1.76$ **(b)** quartet state: $\langle S^2 \rangle = 3.76$

Figure 15: Spin density map of the Au_1-$CO{+}O_2/F^{2+}$-MgO(001) system in the electronic (a) doublet state and (b) quartet state. The upper row shows the systems from above and the bottom row from the side. The spin density boundaries are shown at ± 0.002.

4.3.2 Determination of final states

As mentioned, we will seek a reaction path for the catalytic oxidation of CO by means of NEB method. The determination of final structures and metastable intermediate states is crucial for the results of NEB calculations. As a first step, we performed structure optimizations after the manual insertion of one O atom between the Au-C bond and placing the remaining O atom near the Au atom atop on the Mg ion. The result gives a first indication, why the catalytic oxidation on a single Au atom and also on Au_2 may not work: The remaining O atom goes without any noticeable energy barriers into the vacancy of the MgO(001) surface, a structure that is 4.91 eV more stable in energy than the initial state. The result of the structure optimization is shown in figure 16a. That means that our catalytic cycle on a Au atom deposited on a defective MgO(001) surface will be broken after the first formation of a CO_2 molecule and the remaining O atom will effectively repair the oxygen defect.

Calculations has shown that the Au atom deposited on the defective F^{2+}-MgO(001) has with 1.88 eV the smallest adsorption energy compared to the two other charged systems. Instead of a dissociation of O_2, we observe the molecule does down into the vacancy and pushing away the Au atom together with the adsorbed CO to the next O ion of the MgO(001) surface. This behavior was already observed in previous work [97]. The optimized structure of this alternate final structure is shown in figure 16b. The missing formation of CO_2 makes this structure 1.69 eV higher in energy than the first structure.

An interesting question is what happens with the remaining unpaired electron of the single Au atom. In the case of a defective MgO(001) surface the unpaired electron is mainly located on the Au atom and partially on the adjacent oxygen ions and also on

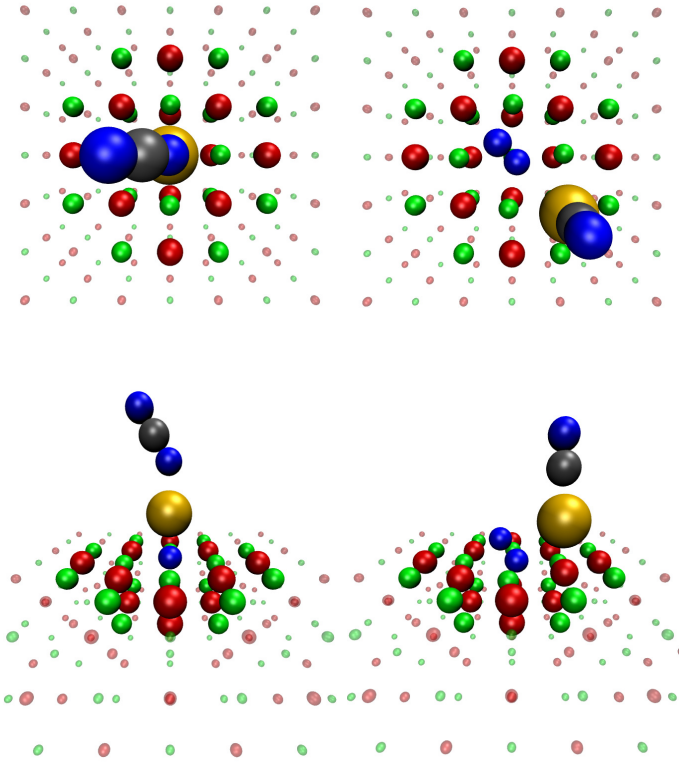

(a) final structure with dissociation of the O_2 molecule

(b) final structure without dissociation of the O_2 molecule

Figure 16: Result of the structure optimizations (a) of the final structure after an insertion of one O atom into the Au-C bond and putting the remaining O atom next to the Au atom and atop on a Mg ion and (b) of the alternative final structure where O_2 goes down into the oxygen vacancy of F^{2+}-MgO(001) without dissociation and the Au atom together with the adsorbed CO is shifted onto the next oxygen ion of the MgO(001) surface. The final structure after the dissociation of O_2 is about 1.69 eV higher in energy than the structure without dissociation. The upper row shows a top view from the structure and the bottom row shows it from the side. The O atoms from the adsorbates are colored blue for clarity, whereas C is colored dark gray.

an adsorbed CO molecule, as we can see in figure 12a. The final structure of figure 16a is in a pure doublet state with a $\langle S^2 \rangle$ expectation value of 0.75. The repair of the defective MgO(001) surface leads to a localization of the unpaired electron at the edge of the cluster as shown in figure 17a. We assume, that the electron will delocalize at the MgO(001) surface, but the embedding scheme leads to this artifact. The deviation in the localization of the unpaired electron causes a different chemical behavior compared to Au atom on a defective MgO(001) surface, so that after the first oxidation step it is not clear if a second catalytic oxidation is still possible. In the case without dissociation, the unpaired electron in the doublet state is located from the π^* orbital of the O_2 molecule and a p orbital of the adjacent oxygen ion. Actually, all 2p orbitals of the O^{2-} ion are completely filled resulting in no unpaired electron. But the Mulliken charge of this oxygen ion is -1.03 with one missing electron in the p orbitals which goes conform with

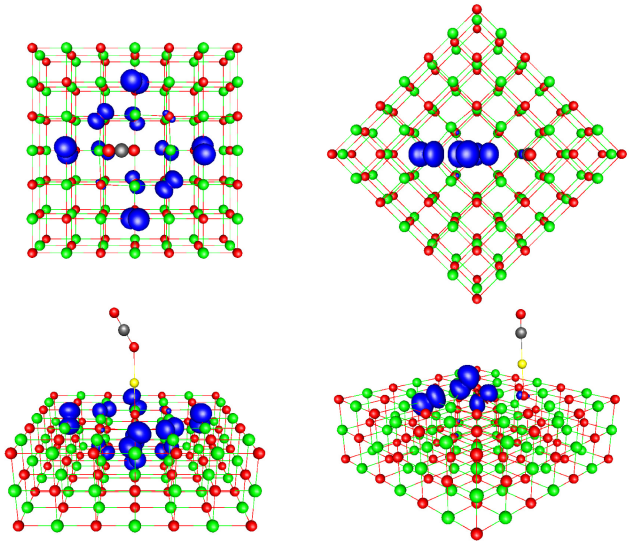

(a) spin density of the final structure after dissociation of the O_2 molecule

(b) spin density of the final structure without dissociation of the O_2 molecule

Figure 17: Spin density maps of the final structure shown in figure 16 respectively. The upper row shows a top view from the spin densities and the bottom row shows it from the side. In (a) the repair of the defective MgO(001) surface by the remaining O atom from the dissociated O_2 leads to a localization of the unpaired electron at the edge of the cluster. If the O_2 molecule goes down into the oxygen vacancy without dissociation it will also result in a doublet state where the unpaired electron is only delocalized in the π^* orbital of O_2 and a p orbital of the adjacent oxygen ion, which corresponds with the remaining negative Mulliken charge of -1.03.

the result of the spin density map in figure 17b.

4.3.3 Reaction path for the oxidation of CO

The NEB method is one possibility to find the minimum energy path or reaction path from one stable configuration to another. In this case the method will be used to find a reaction path for the catalytic oxidation of CO on Au_1/F^{2+}-MgO(001). The initial structure of Au_1-CO+O_2/F^{2+}-MgO(001) is highly spin contaminated, what will potentially result in unreliable estimates for the activation barriers for the first steps on the reaction path until a stronger interaction between the surface and O_2 leads to a pure doublet state. At first the structure in figure 16a will be used as the final configuration for the NEB calculation. The number of calculated images is 20 between the initial and final state, but especially the dissociation of O_2 is described with a higher density of points, so that the size of the steps should not be considered equally spaced. A summary of the results of the NEB calculation is shown in figure 18.

The first step of the catalytic oxidation of CO is the chemisorption of O_2 to the reaction center. In this case it means the movement of O_2 into the F^{2+} vacancy of the MgO(001) surface. The energy barrier from the physisorbed state to this chemisorbed state has a

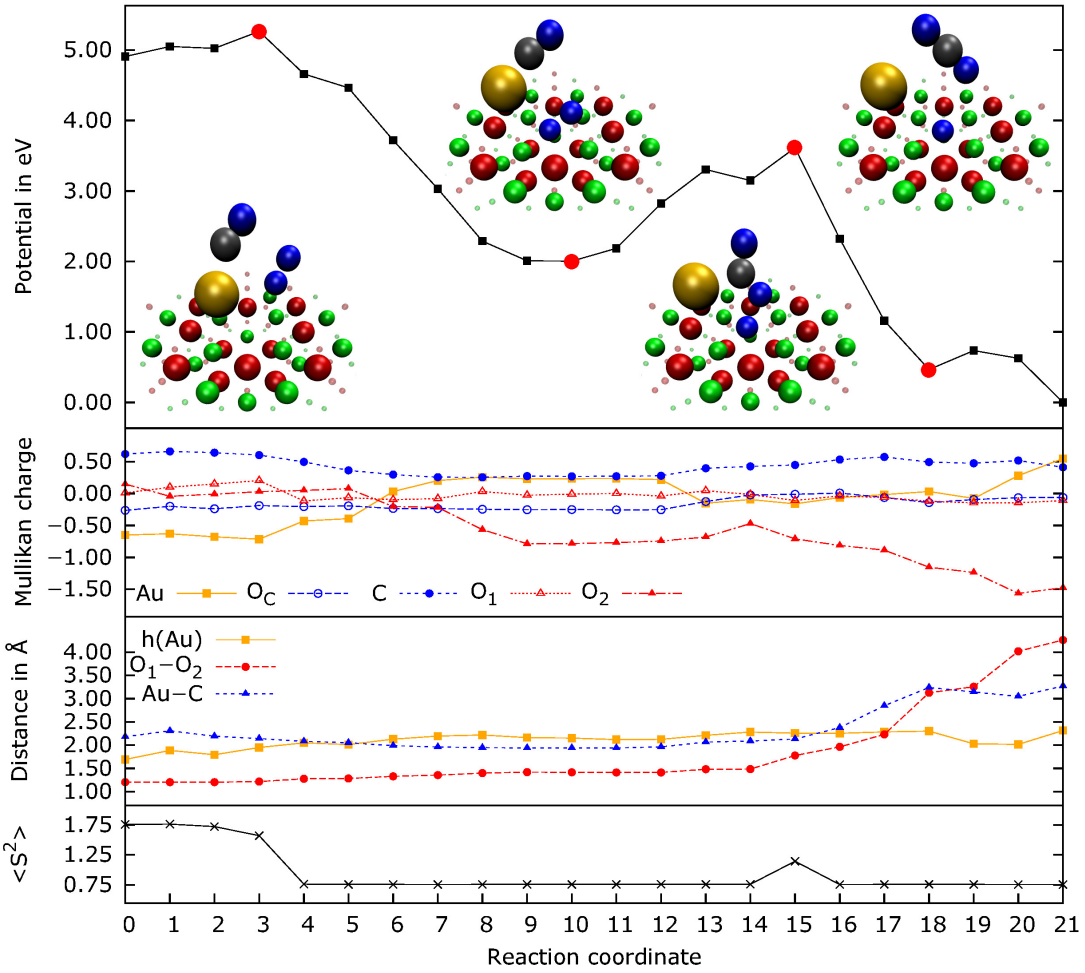

Figure 18: Potential energy (top panel), Mulliken charge (second panel), bond distances (third panel) and the $\langle S^2 \rangle$ expectation value (bottom panel) for the reaction path of the catalytic oxidation of CO with O_2 on Au_1/F^{2+}-MgO(001). The shown structures belong to the red marked points of the upper diagram and are sorted from left to right corresponding to the order of the red marked points respectively. The data are the result of a NEB calculation with 20 points between the initial structure in figure 14 and the final structure in figure 16a. Because of the spin contamination the first energy barrier on step 3, which belongs to the transition from the physisorbed state of O_2 to a chemisorbed state, cannot be fully trusted. The energy minimum at step 9 and 10 is the result of the diffusion of O_2 into the oxygen vacancy from the defective MgO(001) surface, while the Au atom together with the CO adsorbate is partially shifted towards another O ion of the MgO(001) surface. The main energy barrier of 1.61 eV from step 10 to 15 belongs to the dissociation of O_2, but is also influenced by spin contamination with a $\langle S^2 \rangle$ expectation value of $\langle S^2 \rangle_{15} = 1.14$ and can be unreliable. In the second panel it can be seen that the O atom of O_2 which goes into the vacancy gets a negative Mulliken charge, corresponding to an O anion, and the other O atom of O_2 converges with the O atom of CO during the forming of CO_2. The selected structural parameters, such as the height of Au with respect to the height of the first surface layer, the O_2 and Au-C bond length, show the progress of the reaction.

value of 0.36 eV (step 0 $\rightarrow$ step 3), but the high spin contamination makes this result unreliable. Furthermore this process is described with lesser points then necessary for a proper result, so that the true energy barrier could be higher. At step 10 a local minimum is reached which results from the movement of O_2 into the F^{2+} vacancy. This movement supports the following O_2 dissociation by pulling electron density from the MgO(001) surface into the anti-bonding π^* orbitals of O_2. The ensuing weakening of the O-O bond is reflected in the increase of the O-O bond from 1.205 Å at the beginning to 1.419 Å at step 10. The Au atom together with the adsorbed CO molecule is shifted onto the adjacent oxygen ion of the MgO(001) surface. The following dissociation of O_2 has an energy barrier of 1.61 eV (step 10 $\rightarrow$ step 15) but the transition state of step 15 is slightly spin contaminated, with an $\langle S^2 \rangle$ expectation value of $\langle S^2 \rangle_{15} = 1.14$. The potential curve towards this transition state has at step 14 a local minimum which can be caused by the incomplete NEB optimization from the structures of step 10 to step 14 and step 14 to step 18. The last part of the reaction path shows the return of the Au atom onto the central O anion and the adsorption of CO_2 atop on the Au atom. In a periodic MgO(001) surface with indistinguishable oxygen ions on the surface this last step is meaningless. The adsorption of CO_2 atop on the Au atom may happen but because the reaction is highly exothermic ($\Delta E = 4.91$ eV), the excess of energy will probably lead to a desorption of CO_2 into the gas phase. The excess of energy will also lead to a movement of the Au atom and potentially to an agglomeration of gold to one larger cluster.

The evolution of the Mulliken charges follows well to the reaction progress. The charge from the Au atom changes from -0.65, where it is deposited on the F^{2+} vacancy, to $+0.55$ deposited on a surface oxygen ion. We assume that the electron density of the oxygen vacancy strongly overlaps with the atomic orbitals of the Au atom, which make the Mulliken charge more negative than it is probably appropriate. Along the reaction path the Mulliken charge of Au increases to positive values after moving on a surface oxygen ion, whereby the interim decrease between step 13 and 19 is caused by the desorption of CO. The adsorption of CO_2 on the Au atom let the Mulliken charge increases to the final value of $+0.55$. Also along the reaction path, the Mulliken charge of the O atom from O_2, which bonds to the CO molecule, converge to the Mulliken charge of the O atom from CO. The Mulliken charges of the atoms fro CO do not change much during the reaction. The remaining O atom going into the vacancy gets a large negative Mulliken charge of -1.48, which corresponds approximately to the Mulliken charge of the other oxygen ions in the surface. The structural parameters in the third top panel of figure 18 show the reaction progress. A look at the O_2 bond distance at step 15 indicates the bond breaking and the desorption of CO from the Au atom is shown by the increasing Au-C bond at step 16.

To access the quality of the potential curve along the path, further DFT calculations with other functionals (PBE, B2PLYP) were performed. PBE is a generalized gradient approximation method (GGA), which is most frequently used in periodic DFT calculations. B2PLYP is a double-hybrid density functional, where the exchange energy is described by a mixture of the terms derived from GGA functionals and exact exchange from Hartree-Fock functionals. The correlation energy is derived from GGA functionals and Møller-Plesset perturbation theory of second order (MP2). This functional was shown to yield satisfactory results for the adsorption of O_2 on gas phase gold clusters [95]. Figure 19 contains the resulting potential curve obtained using the PBE, B3LYP

B2PLYP functional and as well as the potential curve of the system in an electronic quartet state using the B3LYP functional for the first five steps.

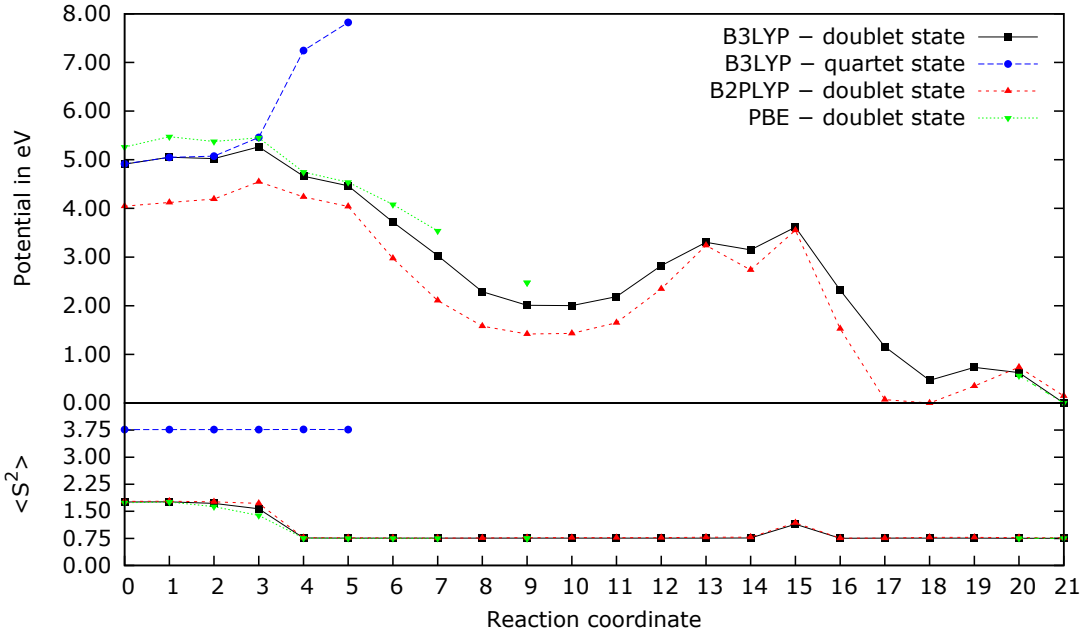

Figure 19: Potential curve and the $\langle S^2 \rangle$ expectation value for the reaction path in figure 18 calculated by different DFT functionals and electronic states. The quartet state of the system using the B3LYP functional shows for the first three steps similar potential energies for the quartet and the spin contaminated doublet state. As the interaction between O_2 and the surface rises, the potential energy increase drastically because of the increasing Pauli repulsion between electrons with the same spin state. B2PLYP gives a similar potential curve but with a higher dissociation energy of O_2 (about 2.13 eV, from step 9 to step 15). PBE failed by converging the wave function of image 7 and image 9 to 19. Except for the quartet state all DFT functionals show the same problem with the spin contamination.

The results of the first five steps calculated by B3LYP in the electronic quartet state show no spin contamination, with an $\langle S^2 \rangle$ expectation value of 3.75. For the first three steps, both the quartet and the spin contaminated doublet state have nearly the same total energy explaining the strong spin contamination of the latter. The system of step 1 in the quartet state shows is even 0.002 eV energetically more favorable than the spin contaminated doublet state. Starting from step 3 the total energy of the quartet state increases drastically because of the increasing Pauli repulsion between the electrons with the same spin state. With the two other DFT functionals one get spin contaminated results as well. The B2PLYP yields a similar potential curve as the B3LYP functional in the electronic doublet state but the dissociation energy of O_2 is with about 2.13 eV (step $9 \rightarrow 15$) higher than the dissociation energy yielding with B3LYP (1.61 eV). Moreover the conformation at step 18, where CO_2 is not adsorbed on the Au atom yet, is lower in energy than the final conformation with adsorbed CO_2. The PBE functional has been getting problem converging the wave function after step 7 where the O_2 gets a larger bond length because of the occupation of the anti-bonding π^* orbitals. This behavior raises strong doubts on the suitability of the PBE functional for systems where the dissociation of O_2 plays an important role.

4.3.4 Alternate reaction path without catalytic oxidation of CO

The movement of the O_2 molecule into the F^{2+} vacancy of the MgO(001) surface without bond breaking and the shifting of the Au-CO cluster onto the adjacent oxygen ion is an alternate path. In the previous reaction path, the O_2 interaction is expected to assist the bond breaking by pulling electrons from the MgO(001) surface into the π^* orbitals of O_2 resulting in a weakening of the O-O bond. Nonetheless the dissociation barrier of about 1.69 eV is still high, so that a dissociation cannot happen. The NEB calculation reveals that the movement of O_2 into the vacancy and the shifting of the Au-CO cluster onto the adjacent oxygen ion is barrierless.

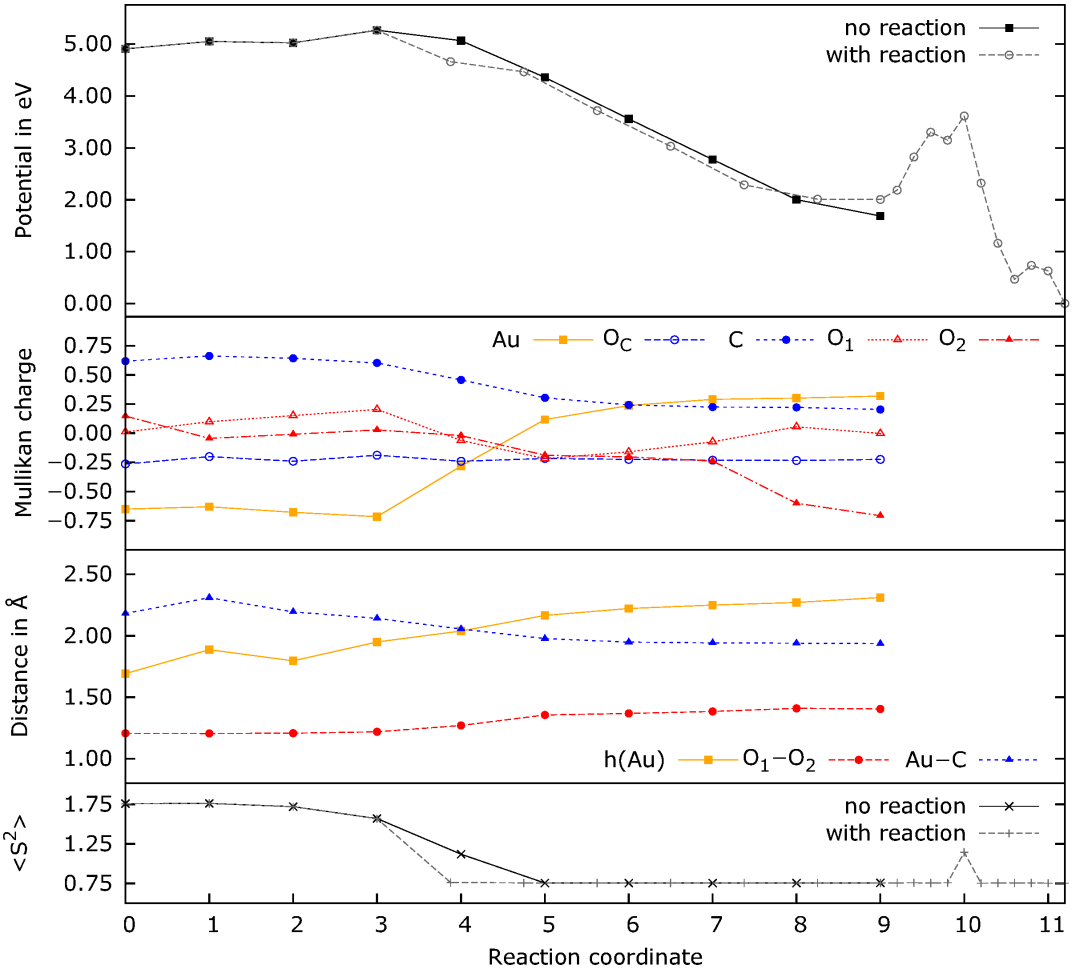

Figure 20: Potential energy (top panel), Mulliken charge (second panel), bond distances (third panel) and the $\langle S^2 \rangle$ expectation value (bottom panel) for the reaction path of the catalytic oxidation of CO with O_2 on Au_1/F^{2+}-MgO(001). The grey potential curve belong to the reaction path of figure 18. Step 3 and 4 marks a barrierless diffusion reaction of the Au-CO shift onto an adjacent O anion and O_2 moves into the vacancy without bond breaking resulting in the conformation of figure 16b.

The potential curve shows that the catalytic oxidation of the adsorbed CO is actually an unlikely process. It is more likely that the O_2 molecule moves into the F^{2+} oxygen vacancy and displace the Au atom onto the adjacent oxygen ion. In the case that the

Au-CO cluster comes back to this filled vacancy the energy barrier for the O_2 dissociation energy is increased to 1.93 eV. Note that the diffusion barrier for a Au atom on MgO(001) is about 0.45 eV. If this corresponds or is higher than the adsorption energy of CO on a Au atom deposited on a clean Mg(001) surface, a catalytic reaction like in figure 18 will be nearly impossible, as the AuCO complex will simply diffuse away. The Mulliken charges show the same behavior as in the reactive case, as well as the bond distances. However, the weakened O-O bond, which is indicated by the increasing O-O bond distance by +0.200 Å, is a result of an electron shift from the defective MgO(001) to the anti-bonding π^* orbitals and shows no dependence on the presence of the Au atom. Therefore the oxidation of one CO molecule with O_2 is probably not dependent on the Au_1/F^{2+}-MgO(001) system itself but on the F^{2+} oxygen vacancy of the defective MgO(001) surface. As it appears, the defective MgO(001) surface will be repaired by the remaining O atom and the catalytic cycle will be broken after a single cycle.

4.4 Catalytic oxidation of CO with O_2 on Au_1/F^{1+}-MgO(001)

The investigation of the single adsorption of CO and O_2 on Au_1/F^{1+}-MgO(001) has shown that neither CO nor O_2 adsorbs strongly on Au_1/F^{1+}-MgO(001). The investigation of a probable structure for a co-adsorption leads to the conformation where the two reactants are adsorbed on the MgO(001) surface next to the Au atom shown in figure 21. The large distances between the Au atom and the adsorbents involve an increase of the inner local part which now includes the adjacent Mg and O ions of the top layer. In consequence the intermediate part is also increased by two atom layers each in the x- and y- direction with a final size of $9 \times 9 \times 3$ in the quantum chemically treated region.

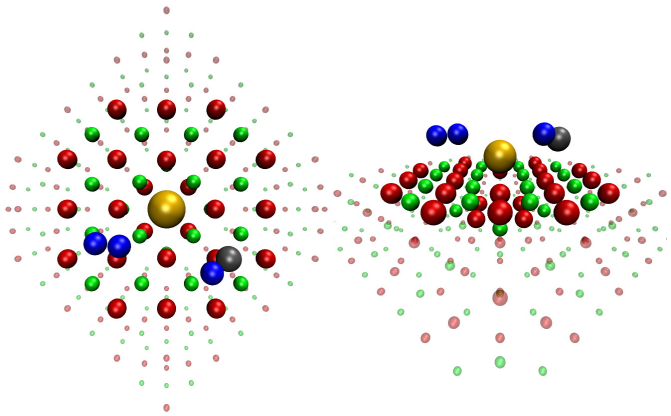

Figure 21: Optimized structures for the co-adsorption of CO and O_2 on Au_1/F^{1+}-MgO(001). The left panel shows a top view from the system and the right panel shows it from the side. The O atoms from the adsorbates are colored blue for clarity, whereas C is colored dark gray. The large distance between the Au atom and the adsorbents are compensated by increasing the inner local part and the intermediate part region to $9 \times 9 \times 3$. As seen for the single adsorbed systems, neither CO nor O_2 shows a high interaction with the central Au_1 cluster.

There is a tiny energetic difference between the two shown structures. The adsorption energies does also remain at 0.20 eV for CO and 0.18 eV for O_2, which is a consequence of the very weak interaction between the adsorbents and the Au atom. Even though

the system is not studied very well, there are two points which are arguments against catalytic activity of the Au_1/F^{1+}-MgO(001) system. On the one side it is likely that there is no strong support for the dissociation of O_2 from the deposited Au_1 cluster because of their weak interaction. On the other side the reaction depends on the presence of CO and O_2 at the Au_1/F^{1+}-MgO(001) cluster. This means a really unlikely reaction of third order. Especially, the small concentration [62] of F^{1+}-MgO(001) defects with one deposited Au_1 cluster inhibits a reaction. Contrary to Au_1/F^{2+}-MgO(001), the Au atom is strongly adsorbed with an adsorption energy of 4.43 eV. That will protect the oxygen vacancy very well against the insertion of an O_2 molecule and the shift of the Au atom onto an adjacent oxygen ion. In view of these thermodynamical and structural properties the catalytic oxidation of CO on Au_1/F^{1+}-MgO(001) was not further studied.

4.5 Catalytic oxidation of CO with O_2 on Au_1/F^0-MgO(001)

The Au_1/F^0-MgO(001) system is a very interesting case. The Au atom is more strongly adsorbed on the oxygen vacancy (3.68 eV), inhibiting the insertion of O_2 into the F^0 vacancy. The energetically favorable adsorption state of O_2 molecule support the π-back-bond resulting in a weakening of the O-O bond. However, this electron saturated system shows a different reaction path as the Au_1/F^{2+}-MgO(001) system, as we will show below, this system is as suitable for a catalytic cycle as the Au_1/F^{2+}-MgO(001) system.

4.5.1 Co-adsorption of CO and O_2 on Au_1/F^0-MgO(001)

Adsorption energies, vibrational frequencies and structural parameters of the single and co-adsorbed system are shown in table 14. The investigation of the single adsorption of O_2 and CO on Au_1/F^0-MgO(001) allows us to define a probable initial guess for the structure for the co-adsorption with a strongly adsorbed O_2 as in figure 11c and a CO adsorbed on the MgO(001) surface next to the Au atom. CO adsorbs either across from the adsorbed O_2 or perpendicular to the plane defined by the Au and O_2. Both assumption results in two energetically stable states, whereby the angled structure in figure 22b is 0.023 eV energetically more favorable than the structure in figure 22a. One can assume that this is the effect of the higher dispersion interaction between the CO and O_2 adsorbents in the angled structure than in the opposite case. The frequency analysis indicates the angled structure as a meta-stable state. One imaginary frequency occurs, which characterizes a vibration of CO parallel to the MgO(001) surface and directed at the adsorbed O_2. After the transition of CO with respect to the imaginary frequency and taking this as an initial structure, the structure optimization results in a carbonate-like state as it is shown in the next section. Table 14 reveals an interesting co-adsorption behavior of the CO adsorbent. The strong interaction between O_2 and the Au atom changes the chemical properties of the former adsorption site, so that the Au-C bond increases by about 1 Å to 3.501 Å. As a consequence, the size of the inner local part must be increased as in the Au_1-CO+O_2/F^{1+}-MgO(001) system to ensure convergence of the calculations. Furthermore, the weaker interaction is also indicated by the lower adsorption energy of 0.25 eV, which is closer to the adsorption energy of CO on a clean

MgO(001) surface, and by the higher vibrational C-O stretch frequency of 2124 cm^{-1}, which is about the C-O stretch frequency in the gas phase (2143 cm^{-1}).

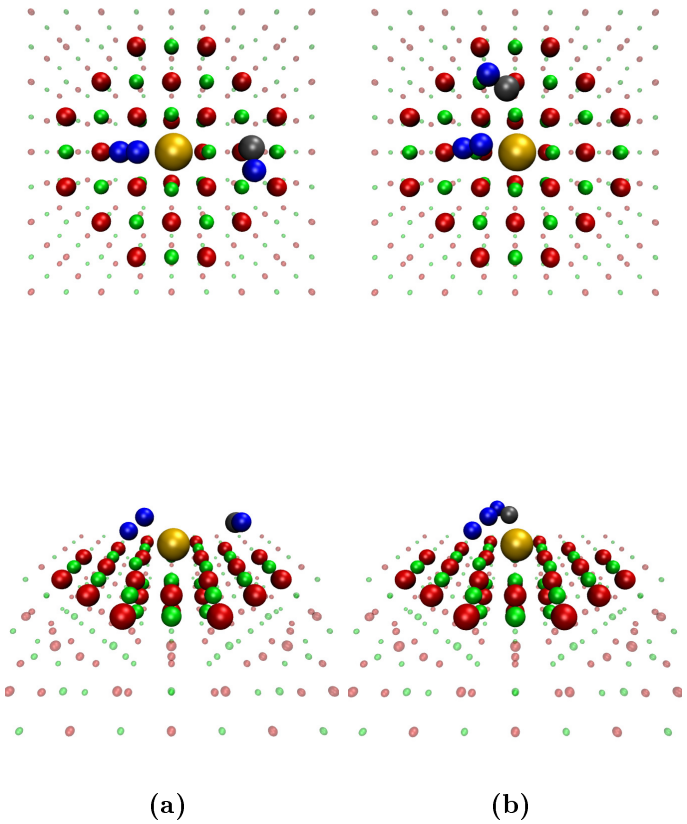

(a) **(b)**

Figure 22: Optimized structures for the co-adsorption of CO and O_2 on Au_1/F^0-MgO(001). The upper row shows a top view from the structure and the bottom row shows it from the side. The O atoms from the adsorbates are colored blue for clarity, whereas C is colored dark gray. The left structure (a) derives from the initial structure with CO across from the strongly adsorbed O_2. The right structure (b), where CO is adsorbed next to O_2, is about 0.023 eV energetically more favorable than (a).

The results show an inverted behavior for the Au_1-CO+O_2/F^{2+}-MgO(001) system, where CO is strongly bound and O_2 diffuses on the surface or arrives directly from the gas phase. In this case O_2 is bonded even more strongly by the Au_1/F^0-MgO(001) cluster and forms a stable precursor state. The CO molecule moves about the MgO(001) surface or directly from the gas phase to this reactive center, because the electron transfer from the electron saturated Au_1/F^0-MgO(001) system to the anti-bonding π^* orbitals of the adsorbed O_2 destabilizes the O-O bond, as can be inferred from the large O-O bond length (1.330 Å). It remains to be clarified, how strongly does the higher adsorption energy of the Au atom on the F^0-MgO(001) vacancy (3.68 eV) prevents the movement of O_2, or how a possible insertion of O into the vacancy could lead to an irreversible breaking of the system.

Table 14: Adsorption energies, vibrational frequencies and structural parameters of single and co-adsorbed system of CO and/or O_2 on Au_1/F^0-MgO(001). Adsorption energies are counterpoise corrected and a scaling factor of 0.970 has been applied to the computed frequencies [80]. The data of the middle column are about the co-adsorbed system with the angled conformation of figure 22b.

system	Au_1-CO/F^0-MgO(001)	Au_1-CO+O_2/F^0-MgO(001)	Au_1-O_2/F^0-MgO(001)
E_{ads}(Au-CO) in eV	0.39	0.25	-
ν(CO) in cm^{-1}	1811	2124	-
r(Au-C) in Å	2.463	3.501	-
r(C-O) in Å	1.159	1.130	-
∠Au-C-O in [°]	139.6	136.2	-
E_{ads}(Au-O_2) in eV	-	1.80	1.81
ν(O-O) in cm^{-1}	-	1153	1149
r(Au-O) in Å	-	2.491	2.450
r(O-O) in Å	-	1.330	1.330
∠Au-O-O in [°]	-	94.5	94.7
$\langle S^2 \rangle$	0.75	0.76	0.76

4.5.2 Determination of transition and final states

The chemistry of CO and O_2 on Au_1/F^{2+}-MgO(001) is very rich and multiple reactions are to be taken into account. In the followings, we proceed to identify the most likely reaction paths for catalytic oxidation of CO on Au_1/F^{2+}-MgO(001). As described above, the structure optimization of the initial structure in figure 22b after the transition of CO with respect to the imaginary frequency results into a carbonate-like state, shown in figure 23. This state is about 3.67 eV energetically more favorable than the initial structure in figure 22b. The carbonate-like structure is nearly trigonal planar (O-C-O angles: 122.7°, 117.1°and 120.2°) and the C-O bond lengths (1.287 Å, 1.279 Å and 1.252 Å) are shorter than in a carbonate ion (1.30 Å) [98].

There are two main hypothesis how the reaction can proceed from the transition structure in figure 23. The first one is inspired by the behavior of CO_2 adsorbed on a clean MgO(001) surface, where it forms also a carbonate-like state with a oxygen ion of the surface [99]. The second one considers the desorption of CO_2 from the carbonate-like structure. In that case the remaining O atom, adsorbed between the Mg cation and the Au atom, can either react with an additional CO molecule to form CO_2 or it can move into the F^0 vacancy of the MgO(001) surface. This mechanism is investigated in section 4.5.4. To the first hypothesis, a possible reaction path can be the movement of the CO_3 structure into the F^0-MgO(001) vacancy by a displacement of the Au atom onto an adjacent O anion of the MgO(001) surface. This reaction path shows similarities to the investigated reaction path of CO and O_2 on Au_1/F^{2+}-MgO(001), but it is uncertain how strong the higher adsorption energy of the Au atom on the F^0-MgO(001) vacancy increases the energy barrier of the process. However, figure 24a shows the mentioned final structure with chemisorbed CO_2 on a repaired MgO(001) surface. Further, experiments have found in addition to the chemisorbed state also a physisorbed state of CO_2 on MgO(001) which

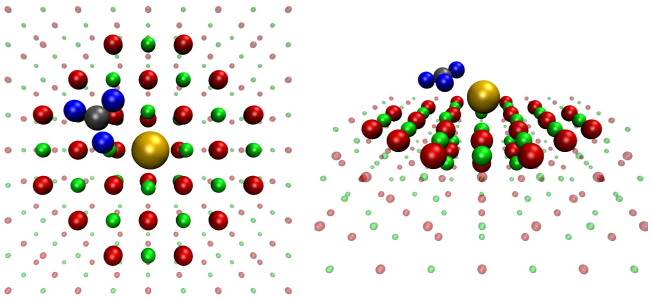

Figure 23: Optimized structure of the carbonate like meta-stable state Au_1-CO_3/F^0-MgO(001). The left panel shows a top view from the system and the right panel shows it from the side. The O atoms from the adsorbates are colored blue for clarity, whereas C is colored dark gray.

is about 0.05 eV higher in energy [100]. This observation can be qualitatively reproduced by the DFT calculations, where figure 24b shows the result of an optimized physisorbed state, which is 0.12 eV higher in energy then the chemisorbed state. Because of the additional Au atom in the calculations similar orders of magnitudes may indicate a comparable behavior in both experiments and theoretical cases.

The next section contains the results of the carbonate-like structure moving into the oxygen vacancy, whereas the reaction channel with the desorption of CO_2 is tackled in section 4.5.4.

4.5.3 Reaction path for the oxidation of CO

To determine the energy barriers for the reaction starting from the initial state in figure 22b over the carbonate like state to the final states of figure 24a and 24b. The results of the NEB calculation are shown in figure 25. The first part of the reaction path until step 6 belongs to the formation of the carbonate-like state. The low energy barrier of 0.34 eV is negligible and the energy barrier may change for different transition vectors of CO. Alternatively, CO can move directly from the gas phase to the adsorbed O_2. The nearly barrier-less formation of the carbonate-like state is caused by the strong π-back donation of the electrons originating from the F^0 vacancy over the Au atom located to the anti-bonding π^* orbitals of the adsorbed O_2. This induces a crucial weakening of the O-O bond and supports the insertion of CO to form the carbonate-like state. The formation of the carbonate-like structure is also reflected by the Mulliken charges of the O atoms, which lie in the range of -0.126 and -0.214 at step 6. Also the O-O distance reflects the dissociation process of O_2. The rate-determining energy barrier belongs to the movement of the carbonate structure into the oxygen vacancy and displacement of the Au atom onto an adjacent O anion. In contrast to the Au_1/F^{2+}-MgO(001) system the adsorption energy of the Au atom is much larger, resulting in an energy barrier of 0.88 eV. This process is accompanied by the increase of the charge of the Au atom moving away from the oxygen vacancy and by the decrease of Mulliken charge of the O atom moving

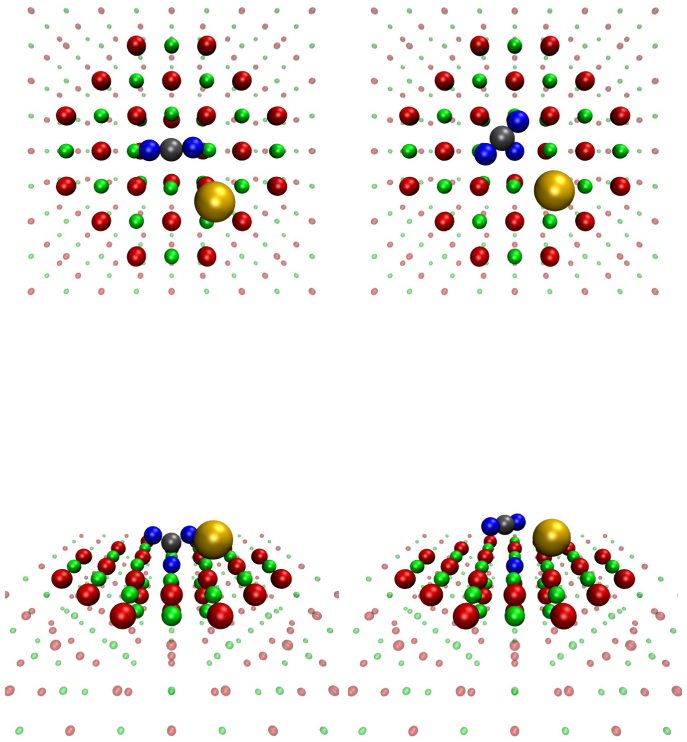

(a) chemical adsorbed state **(b)** physical adsorbed state

Figure 24: Optimized structures of final structures with (a) chemisorbed CO_2 and (b) physisorbed CO_2 on the repaired MgO(001) surface. The upper row shows a top view from the structure and the bottom row shows it from the side. The O atoms from the adsorbates are colored blue for clarity, whereas C is colored dark gray. The physisorbed state is 0.12 eV higher in energy then the chemisorbed state and this adsorption behavior is in a good agreement with experimental results [100].

into the vacancy. The O atom in the vacancy has a charge of -0.867 and only after the transition from chemisorbed CO_2 to physisorbed CO_2 the charge further decrease to -1.368 corresponding to a charge of a surface O anion of the MgO(001) surface. The electron density for the decrease derives from the C atom, which interestingly gets in an even smaller charge then the two bonded O atoms the chemisorbed state, but after the transition to the physisorbed state the C atom get a positive charge of 0.518 and the two bonded O atoms converge at -0.090. The energy barrier for the transition from the chemisorbed to the physisorbed state is 0.32 eV, whereby the physisorbed state is about 0.12 eV higher in energy. During the whole reaction path the $\langle S^2 \rangle$ expectation value stays nearly constant and indicates a pure doublet state of the system.

To investigate if molecular O_2 can move into the oxygen vacancy without any remarkable energy barriers, a NEB calculation was done to determine the potential curve for the movement from the adsorbed state in figure 11c to the state shown in figure 26. The latter was obtained by structure optimization for a geometry biased towards O_2 insertion. The calculation results in a high energy barrier of 1.75 eV, which confirms the hypothesis that the large adsorption energy of one Au atom on the F^0-MgO(001) vacancy inhibit

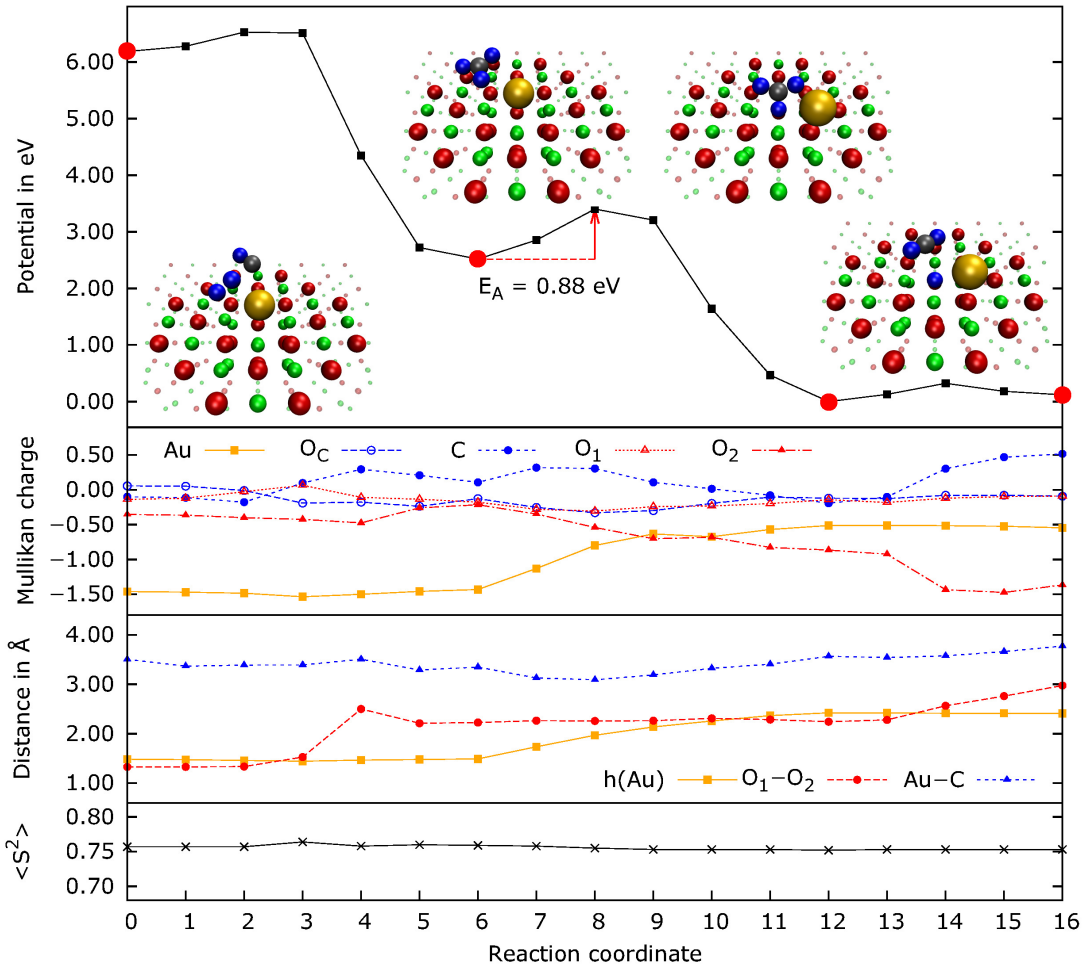

Figure 25: Potential energy (top panel), Mulliken charge (second panel), bond distances (third panel) and the $\langle S^2 \rangle$ expectation value (bottom panel) for the reaction path of the oxidation of CO with O_2 on Au_1/F^0-MgO(001). The shown structures belong to the red marked points of the top panel. The data is the result of a NEB calculation with 15 points between the initial structure in figure 22b and the final structure in figure 24b. The energy minimum at the step 6 is the result of the formation of a carbonate structure. The energy barrier at step 8 with 0.88 eV corresponds to the displacement of the Au atom onto an adjacent oxygen ion and marks the irreversible break of the catalytic cycle. At step 12 the CO_2 is chemisorbed on the O anion, which moved into the F^0 vacancy. For the change into the physisorbed state in step 16 the CO_2 molecule has to overcome an energy barrier of 0.32 eV. The second panel shows, that during the formation of the carbonate like state all O atoms of the adsorbents converge to similar Mulliken charges. During the movement of the bottom O atom into the vacancy, it becomes negatively charged, approximately corresponding to an O anion of the MgO(001) surface. The height of Au with respect to the height of the first surface layer, the O_2 and Au-C bond length show the progress of the reaction. Especially the bond breaking of the O_2 molecule is clearly seen by the change of the O-O bond length at step 4. During the whole reaction path the system remains in a pure doublet state.

the movement of O_2 into the vacancy.

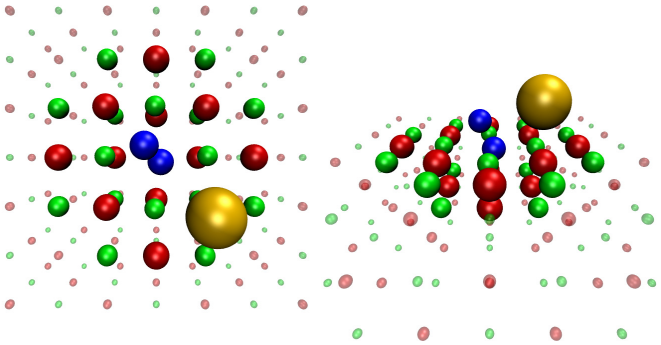

Figure 26: Optimized structure for a final state, if an O_2 molecule moves into the F^0-MgO(001) vacancy and shift the Au_1 cluster onto an adjacent oxygen ion. The left panel shows a top view from the system and the right panel shows it from the side. The O atoms from the adsorbates are colored blue for clarity, whereas C is colored dark gray. This state is about 2.21 eV energetically more favorable but hindered by an energy barrier of 1.75 eV.

In this case we will probably also observe no catalytic oxidation of CO because after the first cycle, the F^0 vacancy is filled by an O anion, which gets his charge from the trapped electrons. Even the stronger adsorption energy of the Au atom on F^0-MgO(001) will not sufficiently protect the vacancy because the insertion of one O atom into the vacancy provides a large energy gain. There is indeed an energy barrier of 0.88 eV but the formation of the carbonate-like state is coupled with an strongly exothermic reaction so that overcoming the barrier should represent no problem. Nevertheless, there is also a second possible reaction path where a CO_2 molecule is cleaved from the carbonate-like structure and the remaining O atom, still bounded between the Mg ion and the Au atom, can react with a further CO molecule.

4.5.4 Alternate reaction paths for the catalytic oxidation of CO

The last investigation of the Au_1/F^0-MgO(001) system deals with the search of a catalytic oxidation cycle, where the vacancy is not be filled by an O atom. Therefore, a reaction path is investigated, where the carbonate-like structure does not move into the vacancy but dissociates to CO_2 and one remaining O atom adsorbed between a surface Mg cation and the Au atom. Afterwards, another CO molecule can be inserted in the catalytic center and reacts with the remaining O atom before dissociating as a newly formed CO_2 molecule. The catalytic cycle would be complete. Figure 27 shows the potential differences and activation barriers calculated by NEB calculations of the mentioned catalytic cycle. For the sake of completeness, other possible mechanism for repairing the surface vacancy are also investigated. The reaction path of figure 25 is similar to the ***B***→***C***→***C′*** path except that the previous section the CO molecule is already adsorbed on the MgO(001) surface in step ***B*** (see figure 27 for labels).

The scheme in figure 27 shows the potential E of the single states, where the clean

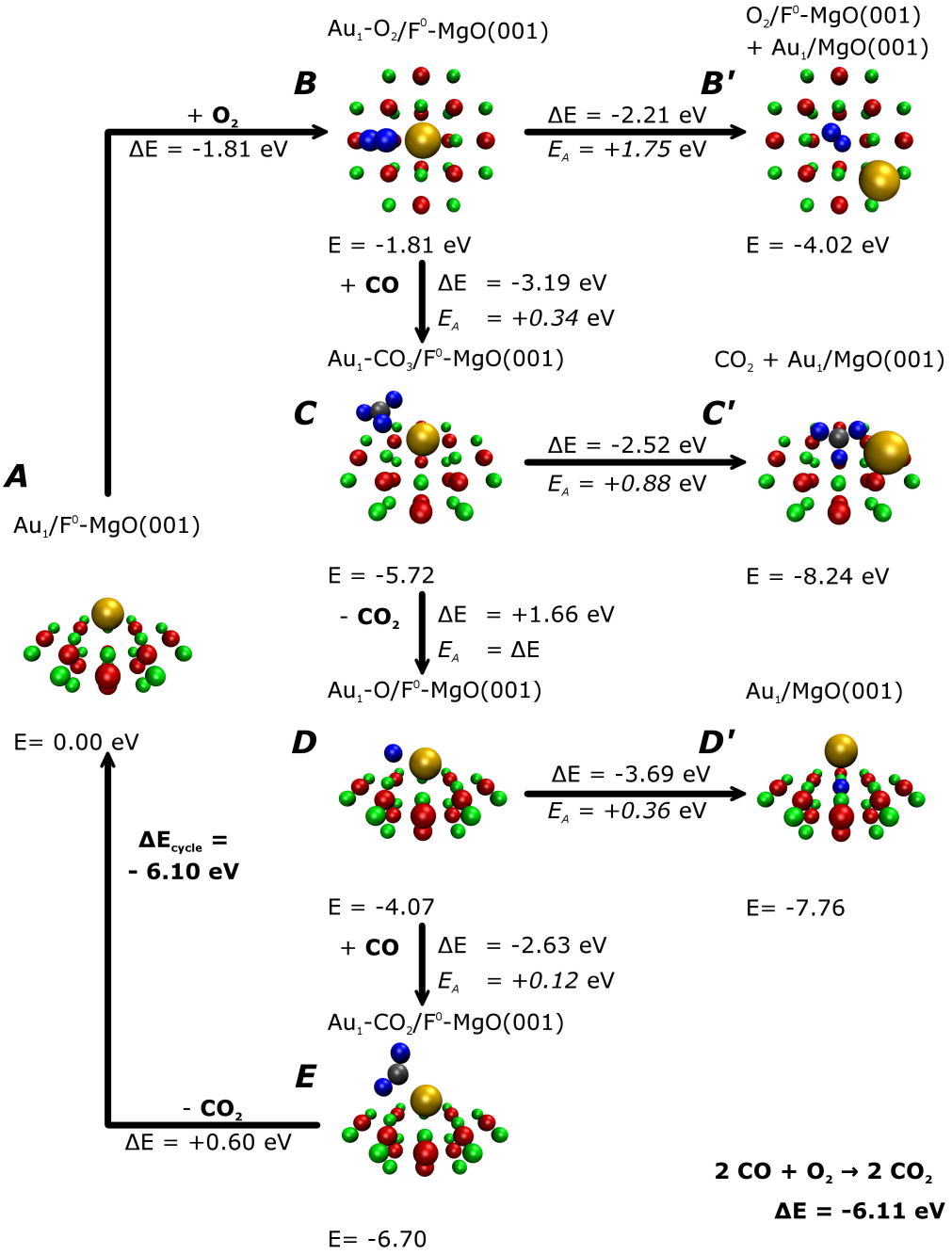

Figure 27: Catalytic oxidation cycle ***A***→***B***→***C***→***D***→***E***→***A*** of two CO molecules with O_2 on Au_1/F^0-MgO(001) and possible termination reactions of the cycle ***B***→***B'***, ***C***→***C'*** and ***D***→***D'*** by repairing the F^0-MgO(001) oxygen vacancy. E belongs to the potential energy of the system where step A is set to zero. ΔE sums up the potential difference between initial and final state and the counterpoise corrected adsorption energy of an incoming or removing molecule if necessary. All single steps are optimized in their structures and are at least meta-stable states. E_A corresponds to the activation barrier resulting from NEB calculations. The net potential difference after one cycle E_{cycle} converge to the net potential difference of the reaction shown in the bottom right corner.

Au_1/F^0-MgO(001) system in ***A*** is set to zero. For the potential energy difference ΔE involving addition or removal of a molecule between initial and final state, the counterpoise corrected adsorption energy is taken into account. For example, the potential energy difference of reaction ***B***→***C*** involves the counterpoise corrected adsorption energy of CO to the optimized position like the initial state in figure 22b and the difference in the total energy of the initially adsorbed state and the carbonate-like state. The shown activation barriers E_A results from NEB calculations. The activation barriers of ***B***→***C*** and ***C***→***C'*** are taken from the results in figure 25, whereby the other values results from NEB calculation with 5 steps between the initial and final state.

The first process ***A***→***B*** shows the adsorption of O_2 on Au_1/F^0-MgO(001) and is chosen as a precursor because of the high adsorption energy of 1.81 eV. As mentioned above, the movement of the adsorbed O_2 molecule into the F^0-MgO(001) vacancy (***B***→***B'***) has a high activation barrier because of the strong adsorption of both O_2 on Au_1/F^0-MgO(001) and Au_1 on the F^0-MgO(001) vacancy. The low activation barrier of +0.34 eV and the high energy gain of −3.19 eV by the formation of the carbonate-like state in ***C*** singles out this process as the dominants reaction path. Actually, the energy difference and the activation barriers of the processes ***C***→***C'*** and ***C***→***D*** clearly favor the movement of the carbonate-like structure into the oxygen vacancy because the dissociation of CO_2 requires around twice as much activation energy (+1.66 eV) as the reparation of the oxygen vacancy (0.88 eV). The high excess energy from the formation of the carbonate-like structure particularly supports the movement into the vacancy, especially if the momentum of an incoming CO molecule does also go towards the oxygen vacancy. It appears that the path ***A***→***B***→***C***→***C'*** in figure 27 is the dominant and the most probable reaction path. Furthermore the next bifurcation from ***D*** to ***D'*** or ***E*** has in both ways small activation energies of +0.36 eV for the movement of the O atom into the vacancy and +0.12 eV for the formation of CO_2. Nevertheless the small activation barrier for the movement of the single O atom into the vacancy is difficult to prevent and will be a reason for an irreversible breaking of the catalytic cycle. The finally desorption of CO_2 from ***E*** back to ***A*** has an additional barrier of only 0.60 eV.

The reaction path over ***A***→***B***→***C***→***D***→***E***→***A*** corresponds to a catalytic cycle for the oxidation of two CO molecules with O_2 to two CO_2 molecules. The final potential difference of −6.10 eV after one cycle matches with the energy difference of the net reaction shown in the bottom right corner of figure 27 resulting from the difference of the single point energies of the optimized structures calculated using the same B3LYP functional. The negligible deviation can be reasoned by errors from the basis set superposition error, where the counterpoise correction is not always exact, and inconsistency of the system size using both the $7 \times 7 \times 3$ and $9 \times 9 \times 3$ systems to describe the F^0-MgO(001) surface of the quantum mechanical treated region in some cases.

In the end, a catalytic oxidation cycle on the Au_1/F^0-MgO(001) surface appears also difficult to perform. The possibilities to break the catalytic cycle are very probable, or as it is shown in the case between ***C***→***D*** or ***C***→***C'***, even most favorable. Nevertheless, it could be conceivable that the dissociation of CO_2 in ***C***→***D*** can be excited by laser irradiation. Frequency analysis of the structure ***C*** results in a symmetric stretch frequency for the carbonate-like structure with $\nu_s(CO_3) = 1039\ cm^{-1}$, as well as $\nu_{as}^{(1)}(CO_3) = 1300\ cm^{-1}$ and $\nu_{as}^{(2)}(CO_3) = 1183\ cm^{-1}$ for the antisymmetric stretch frequencies. A laser irradiation at the $\nu_{as}^{(1)}$ frequency could favor the dissociation of CO_2 and simultaneously prevent the

reparation of the oxygen vacancy. In this scenario, the realization of a catalytic oxidation cycle would be possible, although it would remain margin in view of the thermodynamical analysis presented in this section.

5 Conclusion and Outlook

Experiments from Landmann et al. [19] show no catalytic activity of Au_1 and Au_2 clusters deposited on defect-rich MgO(001) surfaces, whereas Au_{3-7} clusters shows a limited and $Au_{n\geq 8}$ shows a high catalytic activity for the oxidation of CO. In the framework of this thesis we investigated reasons for the lack of catalytic activity of the $Au_{1,2}$ clusters deposited on $F^{2+,1+,0}$-MgO(001) surfaces. The Au_1 cluster are not strongly adsorbed on F^{2+}- and F^0-MgO(001) to protect the oxygen vacancy efficiently resulting in the irreversible break of the catalytic system. Especially, Au_1 on F^{2+}-MgO(001) is so weakly adsorbed (1.88 eV), that there is only a negligible activation barrier for the strongly exothermic reaction path of the concerted movement of O_2 into the vacancy and displacement of the Au atom onto an adjacent O anion. Only the Au_1 is strongly adsorbed on the oxygen vacancy of the F^{1+}-MgO(001) surface (4.43 eV) inhibiting the repair of the vacancy due to a high energy barrier. The system shows no strong interaction with both CO and O_2. Thus, there is no support for the cluster-mediated bond breaking of O_2, which marks the rate-determining process for the oxidation of CO. In the case of Au_1 adsorbed on F^0-MgO(001) a strong interaction between adsorbed O_2 and the surface system leads to a strong π-back-bond from the Au atom to the anti-bonding π^* molecular orbitals of O_2 and a weakening of the O-O bond. The bond weakening supports the insertion of CO and the formation of a carbonate-like structure adsorbed next to the Au atom on the MgO(001) surface. Even though the Au_1 cluster is more strongly adsorbed on F^0-MgO(001) (3.68 eV) as in the Au_1/F^{2+}-MgO(001) system, the energy barrier (0.88 eV) for the movement of a O atom of the carbonate-like structure while displacing the Au atom onto an adjacent O anion is not large enough to efficiently protect the vacancy. One way to preserve the catalytic cycle is by dissociating CO_2 from the carbonate-like structure. The energy needed for the dissociation (1.66 eV) is found to be almost twice as high as the reparation of the oxygen vacancy, thus marking the irreversible breaking of the catalytic cycle after the first formation of CO_2 the most probable reaction path.

The Au_2 clusters deposited on defective MgO(001) seem difficult to handle using the PEEC method with the chosen parameters. The inclusion of DFT-D3 dispersion correction, necessary for a proper description of the physisorption behavior of O_2, leads to a lateral displacement and a diffusion of the upper Au atom. Nevertheless, without DFT-D3 dispersion correction calculations results into a medium (0.47 eV) and a weak (0.12 eV) adsorption strength for O_2 on Au_2/F^{2+}-MgO(001) and Au_2/F^{1+}-MgO(001). Without the support of weakening the O-O bond like in Au_1-O_2/F^{2+}-MgO(001), the energy barrier for the oxidation of CO remains large. In case of O_2 adsorbed on Au_2/F^0-MgO(001), we could not identify a stable adsorption state. Due to the highly intricate adsorption behavior, which we could not resolve using the present set-ups, investigations about reaction paths for the oxidation of CO on Au_2 deposited on defect-rich MgO(001) were not performed.

In case of physisorbed O_2 (two unpaired electrons in the electronic ground state) on a gold cluster with an odd number of electrons, the results of system in the electronic doublet state (low-spin state) became highly spin contaminated. This is caused by the similar energies of the low-spin doublet state and the high-spin quartet state. Due to the Pauli principle, the high-spin state leads to no spin contaminated results but they become

energetically more unfavorable than the low-spin state by increasing O_2-Au interaction. Consequentially, systems with chemisorbed O_2 do not show spin contaminated results in the electronic doublet state.

It generally seems that catalytic activity on Au_1 and Au_2 supported clusters is not possible, either because the cluster is unstable or the cycle is broken along the way or the system does not support the bond breaking of O_2.

An interesting question will be, if the weak catalytic activity of the Au_{3-7} clusters starting with the smallest Au_3 can be qualitatively reproduced by the theoretical investigation using the same methodology. If the results corresponds to the experimental observations, the suitability of the chosen method to describe the Au adsorbed defective MgO(001) surface will be proven. Increasing of the cluster size will open even more probable reaction channels along a large amount of degrees of freedom making these future considerations extremely expensive computationally.

References

[1] D. Cha, G. Parravano, *Journal of Catalysis* **1970**, *18*, 200 –211.

[2] G. C. Bond, P. A. Sermon, G. Webb, D. A. Buchanan, P. B. Wells, *J. Chem. Soc. Chem. Commun.* **1973**, 444b–445.

[3] H. Huber, D. McIntosh, G. A. Ozin, *Inorganic Chemistry* **1977**, *16*, 975–979.

[4] M. Haruta, T. Kobayashi, H. Sano, N. Yamada, *Chemistry Letters* **1987**, *16*, 405–408.

[5] M. Haruta, N. Yamada, T. Kobayashi, S. Iijima, *Journal of Catalysis* **1989**, *115*, 301 –309.

[6] M. Haruta, English, *Gold Bulletin* **2004**, *37*, 27–36.

[7] M. Haruta, *Catalysis Today* **1997**, *36*, Copper, Silver and Gold in Catalysis, 153 –166.

[8] P. Pyykkö, *Angewandte Chemie International Edition* **2004**, *43*, 4412–4456.

[9] L. D. Socaciu, J. Hagen, T. M. Bernhardt, L. Wöste, U. Heiz, H. Häkkinen, U. Landman, *Journal of the American Chemical Society* **2003**, *125*, PMID: 12926969, 10437–10445.

[10] G. Pacchioni, L. Giordano, M. Baistrocchi, *Phys. Rev. Lett.* **June 2005**, *94*, 226104.

[11] B. Yoon, H. Häkkinen, U. Landman, A. S. Wörz, J.-M. Antonietti, S. Abbet, K. Judai, U. Heiz, *Science* **2005**, *307*, 403–407.

[12] A. Del Vitto, G. Pacchioni, F. Delbecq, P. Sautet, *The Journal of Physical Chemistry B* **2005**, *109*, PMID: 16851939, 8040–8048.

[13] P Frondelius, H Häkkinen, K Honkala, *New Journal of Physics* **2007**, *9*, 339.

[14] P. Frondelius, H. Häkkinen, K. Honkala, *Phys. Rev. B* **Aug. 2007**, *76*, 073406.

[15] M. Sterrer, T. Risse, M. Heyde, H.-P. Rust, H.-J. Freund, *Phys. Rev. Lett.* **May 2007**, *98*, 206103.

[16] S. Schintke, S. Messerli, M. Pivetta, F. m. c. Patthey, L. Libioulle, M. Stengel, A. De Vita, W.-D. Schneider, *Phys. Rev. Lett.* **Dec. 2001**, *87*, 276801.

[17] A. Sanchez, S. Abbet, U. Heiz, W.-D. Schneider, H. Häkkinen, R. N. Barnett, U. Landman, *The Journal of Physical Chemistry A* **1999**, *103*, 9573–9578.

[18] M. Arenz, U. Landman, U. Heiz, *ChemPhysChem* **2006**, *7*, 1871–1879.

[19] U. Landman, B. Yoon, C. Zhang, U. Heiz, M. Arenz, English, *Topics in Catalysis* **2007**, *44*, 145–158.

[20] H. Häkkinen, S. Abbet, A. Sanchez, U. Heiz, U. Landman, *Angewandte Chemie International Edition* **2003**, *42*, 1297–1300.

[21] A. M. Burow, M. Sierka, J. Döbler, J. Sauer, *The Journal of Chemical Physics* **2009**, *130*, 174710.

[22] E. Schrödinger, *Phys. Rev.* **1926**, *28*, 1049–1070.

[23] P. Hohenberg, W. Kohn, *Phys. Rev.* **1964**, *136*, B864–B871.

[24] W. Kohn, L. J. Sham, *Phys. Rev.* **1965**, *140*, A1133–A1138.

[25] M. Born, R. Oppenheimer, *Annalen der Physik* **1927**, *389*, 457–484.

[26] W. Koch, M. Holthausen, *A chemist's guide to density functional theory*, Wiley-VCH, Weinheim, New York, Chichester, **2001**.

[27] J. C. Slater, *Phys. Rev.* **1929**, *34*, 1293–1322.

[28] I. N. Levine, *Quantum Chemistry*, Prentice-Hall, 5th ed., **2000**.

[29] S. H. Vosko, L. Wilk, M. Nusair, *Canadian Journal of Physics* **1980**, *58*, 1200–1211.

[30] J. P. Perdew, K. Burke, M. Ernzerhof, *Phys. Rev. Lett.* **1996**, *77*, 3865–3868.

[31] J. P. Perdew, K. Burke, M. Ernzerhof, *Phys. Rev. Lett.* **1997**, *78*, 1396–1396.

[32] F. Jensen, *Introduction to Computational Chemistry*, Wiley-VCH, 2nd ed., **2007**.

[33] A. D. Becke, *The Journal of Chemical Physics* **1993**, *98*, 5648–5652.

[34] C. Lee, W. Yang, R. G. Parr, *Phys. Rev. B* **1988**, *37*, 785–789.

[35] W. Koch, M. Holthausen, *A Chemist's Guide to Density Functional Theory*, Wiley-VCH, 2nd ed., **2001**.

[36] J. A. Pople, P. M. W. Gill, N. C. Handy, *International Journal of Quantum Chemistry* **1995**, *56*, 303–305.

[37] O. Gunnarsson, B. I. Lundqvist, *Phys. Rev. B* **1976**, *13*, 4274–4298.

[38] S. Grimme, *Journal of Computational Chemistry* **2004**, *25*, 1463–1473.

[39] S. Grimme, J. Antony, S. Ehrlich, H. Krieg, *The Journal of Chemical Physics* **2010**, *132*, 154104.

[40] S. F. Boys, *Proceedings of the Royal Society of London A: Mathematical Physical and Engineering Sciences* **1950**, *200*, 542–554.

[41] R. Dronskowski, R. Hoffmann, *Computational Chemistry of Solid State Materials: A Guide for Materials Scientists, Chemists, Physicists and Others*, Wiley-VCH, Weinheim, **2005**.

[42] H. Hellmann, *The Journal of Chemical Physics* **1935**, *3*, 61–61.

[43] K. N. Kudin, G. E. Scuseria, *Chemical Physics Letters* **1998**, *283*, 61–68.

[44] L. Greengard, V. Rokhlin, *Journal of Computational Physics* **1987**, *73*, 325–348.

[45] L. Greengard, *The Rapid evaluation of potential fields in particle systems*, Cambridge, Mass. MIT Press, **1988**.

[46] G. J. Iverson, G. Mack, *Annals of Physics* **1971**, *64*, 211–253.

[47] C. Kittel, *Introduction to Solid State Physics*, Wiley-VCH, 7th ed., **1996**.

[48] J. Nichols, H. Taylor, P. Schmidt, J. Simons, *The Journal of Chemical Physics* **1990**, *92*, 340–346.

[49] Turbomole Version 6.5 USER'S MANUAL, Turbomole GmbH, **2013**.

[50] F. Jensen, *The Journal of Chemical Physics* **1995**, *102*, 6706–6718.

[51] W. H. Miller, N. C. Handy, J. E. Adams, *The Journal of Chemical Physics* **1980**, *72*, 99–112.

[52] H. Jónsson, G. Mills, K. W. Jacobsen in *Classical and quantum dynamics in condensed phase simulations*, World Scientific, **1998**, Chapter 16, pp. 385–404.

[53] G. Henkelman, H. Jónsson, *The Journal of Chemical Physics* **2000**, *113*, 9978–9985.

[54] H. Group, Saddle Point Finding Methods, http://theory.cm.utexas.edu/henkelman/research/saddle/, (13/03/2015).

[55] G. Henkelman, B. P. Uberuaga, H. Jónsson, *The Journal of Chemical Physics* **2000**, *113*, 9901–9904.

[56] English in *II-VI and I-VII Compounds; Semimagnetic Compounds*, (Eds.: O. Madelung, U. Rössler, M. Schulz), Landolt-Börnstein - Group III Condensed Matter, Springer Berlin Heidelberg, **1999**, pp. 1–6.

[57] G. Pacchioni, H. Freund, *Chemical Reviews* **2013**, *113*, PMID: 23116191, 4035–4072.

[58] R. Whited, C. J. Flaten, W. Walker, *Solid State Communications* **1973**, *13*, 1903–1905.

[59] G. Pacchioni, C. Sousa, F. Illas, F. Parmigiani, P. S. Bagus, *Phys. Rev. B* **1993**, *48*, 11573–11582.

[60] L. Tjeng, A. Vos, G. Sawatzky, *Surface Science* **1990**, *235*, 269–279.

[61] E. Giamello, P. Ugliengo, E. Garrone, *J. Chem. Soc. Faraday Trans. 1* **1989**, *85*, 1373–1382.

[62] M. Sterrer, E. Fischbach, M. Heyde, N. Nilius, H.-P. Rust, T. Risse, H.-J. Freund, *The Journal of Physical Chemistry B* **2006**, *110*, PMID: 16640421, 8665–8669.

[63] E. Scorza, U. Birkenheuer, C. Pisani, *The Journal of Chemical Physics* **1997**, *107*, 9645–9658.

[64] A. Tench, *Surface Science* **1971**, *25*, 625–632.

[65] R. L. Nelson, J. W. Hale, *Discuss. Faraday Soc.* **1971**, *52*, 77–88.

[66] R. R. Sharma, A. M. Stoneham, *J. Chem. Soc. Faraday Trans. 2* **1976**, *72*, 913–919.

[67] A. M. Ferrari, G. Pacchioni, *The Journal of Physical Chemistry* **1995**, *99*, 17010–17018.

[68] S. Abbet, A. Sanchez, U. Heiz, W.-D. Schneider, A. M. Ferrari, G. Pacchioni, N. Rösch, *Journal of the American Chemical Society* **2000**, *122*, 3453–3457.

[69] U. Heiz, E. L. Bullock, *J. Mater. Chem.* **2004**, *14*, 564–577.

[70] B. Yoon, H. Häkkinen, U. Landman, A. S. Wörz, J.-M. Antonietti, S. Abbet, K. Judai, U. Heiz, *Science* **2005**, *307*, 403–407.

[71] O. Treutler, R. Ahlrichs, *The Journal of Chemical Physics* **1995**, *102*, 346–354.

[72] M. Von Arnim, R. Ahlrichs, *Journal of Computational Chemistry* **1998**, *19*, 1746–1757.

[73] S. R. Bahn, K. W. Jacobsen, English, *Comput. Sci. Eng.* **2002**, *4*, 56–66.

[74] P. J. Hay, W. R. Wadt, *The Journal of Chemical Physics* **1985**, *82*, 270–283.

[75] A. D. McLean, G. S. Chandler, *The Journal of Chemical Physics* **1980**, *72*, 5639–5648.

[76] P. Hariharan, J. Pople, English, *Theoretica chimica acta* **1973**, *28*, 213–222.

[77] T. Clark, J. Chandrasekhar, G. W. Spitznagel, P. V. R. Schleyer, *Journal of Computational Chemistry* **1983**, *4*, 294–301.

[78] P. J. Hay, W. R. Wadt, *The Journal of Chemical Physics* **1985**, *82*, 299–310.

[79] S. Boys, F. Bernardi, *Molecular Physics* **1970**, *19*, 553–566.

[80] National Institute of Standards and Technology, Precomputed vibrational scaling factors, `http://cccbdb.nist.gov/vibscalejust.asp`, Online, accessed 11/04/2008.

[81] E. Bitzek, P. Koskinen, F. Gähler, M. Moseler, P. Gumbsch, *Phys. Rev. Lett.* **2006**, *97*, 170201.

[82] W. Humphrey, A. Dalke, K. Schulten, *Journal of Molecular Graphics* **1996**, *14*, 33–38.

[83] J. Stone, MA thesis, Computer Science Department, University of Missouri-Rolla, **1998**.

[84] G. Hermann, V. Pohl, A. Schild, orbkit: A Toolbox for Post-Processing Quantum Chemical Wavefunction Data, http://sourceforge.net/p/orbkit, 0.2.0, **2014**.

[85] L. Laaksonen, gOpenMol: Program for the display and analysis of molecular structures, 3.0, **2004**.

[86] T Williams, C Kelley, many others, gnuplot 4.6, http://www.gnuplot.info, **2012**.

[87] T. G. Team, GIMP 2.8.10, www.gimp.org, **2014**.

[88] M. A. Brown, F. Ringleb, Y. Fujimori, M. Sterrer, H.-J. Freund, G. Preda, G. Pacchioni, *The Journal of Physical Chemistry C* **2011**, *115*, 10114–10124.

[89] MATLAB, version 7.12.0 (R2011a), The MathWorks Inc. **2011**.

[90] R. Wichtendahl, M. Rodriguez-Rodrigo, U. Härtel, H. Kuhlenbeck, H.-J. Freund, *physica status solidi (a)* **1999**, *173*, 93–100.

[91] H. Jian-Wei, C. A. Estrada, J. S. Corneille, W. Ming-Cheng, D. W. Goodman, *Surface Science* **1992**, *261*, 164 –170.

[92] L. Giordano, J. Carrasco, C. Di Valentin, F. Illas, G. Pacchioni, *The Journal of Chemical Physics* **2006**, *124*, 174709.

[93] R. Wichtendahl, M. Rodriguez-Rodrigo, U. Härtel, H. Kuhlenbeck, H.-J. Freund, *Surface Science* **1999**, *423*, 90–98.

[94] L. Kantorovich, M. Gillan, *Surface Science* **1997**, *374*, 373 –386.

[95] H.-C. Fang, Z. H. Li, K.-N. Fan, *Phys. Chem. Chem. Phys.* **2011**, *13*, 13358–13369.

[96] G. Mills, M. S. Gordon, H. Metiu, *The Journal of Chemical Physics* **2003**, *118*, 4198–4205.

[97] G. Geneste, J. Morillo, F. Finocchi, *The Journal of Chemical Physics* **2005**, *122*, 174707.

[98] A. F. Holleman, N. Wiberg, *Lehrbuch der Anorganischen Chemie*, de Gruyter, 102nd ed., **2007**.

[99] M. B. Jensen, L. G. M. Pettersson, O. Swang, U. Olsbye, *The Journal of Physical Chemistry B* **2005**, *109*, PMID: 16853136, 16774–16781.

[100] D. Meixner, D. Arthur, S. George, *Surface Science* **1992**, *261*, 141 –154.